JBC RESEARCH ARTICLE

A novel calcium channel Cavβ$_2$ splice variant with unique properties predominates in the retina

Received for publication, August 19, 2022, and in revised form, January 15, 2023 Published, Papers in Press, February 2, 2023,
https://doi.org/10.1016/j.jbc.2023.102972

Hartwig Seitter[1,*], **Jana Obkircher**[1], **Patricia Grabher**[1], **Julia Hartl**[1], **Lucia Zanetti**[1], **Uwe Thorsten Lux**[2], **Georgios Fotakis**[3], **Monica L. Fernández-Quintero**[4], **Teresa Kaserer**[5], **and Alexandra Koschak**[1,*]

From the [1]*Department of Pharmacology and Toxicology, Institute of Pharmacy, University of Innsbruck, Innsbruck, Austria;* [2]*Department of Biology, Animal Physiology/Neurobiology, Friedrich-Alexander-University Erlangen-Nürnberg, Erlangen, Germany;* [3]*Institute of Bioinformatics, Medical University of Innsbruck, Innsbruck, Austria;* [4]*Institute of General, Inorganic and Theoretical Chemistry, and* [5]*Department of Pharmaceutical Chemistry, Institute of Pharmacy, University of Innsbruck, Innsbruck, Austria*

Reviewed by members of the JBC Editorial Board. Edited by Kirill Martemyanov

Cavβ subunits are essential for surface expression of voltage-gated calcium channel complexes and crucially modulate biophysical properties like voltage-dependent inactivation. Here, we describe the discovery and characterization of a novel Cavβ$_2$ variant with distinct features that predominates in the retina. We determined spliced exons in retinal transcripts of the *Cacnb2* gene, coding for Cavβ$_2$, by RNA-Seq data analysis and quantitative PCR. We cloned a novel Cavβ$_2$ splice variant from mouse retina, which we are calling β$_{2i}$, and investigated biophysical properties of calcium currents with this variant in a heterologous expression system as well as its intrinsic membrane interaction when expressed alone. Our data showed that β$_{2i}$ predominated in the retina with expression in photoreceptors and bipolar cells. Furthermore, we observed that the β$_{2i}$ N-terminus exhibited an extraordinary concentration of hydrophobic residues, a distinct feature not seen in canonical variants. The biophysical properties resembled known membrane-associated variants, and β$_{2i}$ exhibited both a strong membrane association and a propensity for clustering, which depended on hydrophobic residues in its N-terminus. We considered available Cavβ structure data to elucidate potential mechanisms underlying the observed characteristics but resolved N-terminus structures were lacking and thus, precluded clear conclusions. With this description of a novel N-terminus variant of Cavβ$_2$, we expand the scope of functional variation through N-terminal splicing with a distinct form of membrane attachment. Further investigation of the molecular mechanisms underlying the features of β$_{2i}$ could provide new angles on the way Cavβ subunits modulate Ca^{2+} channels at the plasma membrane.

Voltage-gated calcium (Ca^{2+}) channel Cavβ subunits (Cavβ) are cytosolic auxiliary subunits that play an essential role in regulating the surface expression and gating properties of voltage-gated Ca^{2+} channels (VGCC). As critical modulators of VGCC properties, they act by increasing open probability, hyperpolarizing the voltage dependence of activation (1), and increasing the number of channels on the plasma membrane *via* different mechanisms (2) thus enhancing macroscopic Ca^{2+} currents several-fold. Importantly, all Cavβ subunits also enhance voltage-dependent inactivation (VDI), with the notable exception of splice variants β$_{2a}$ and β$_{2e}$ that show the opposite effect, slowing down, and decreasing VDI (3).

As part of the membrane-associated guanylate kinase protein family, Cavβ subunits are cytoplasmic proteins that contain a conserved Src homology 3 (SH3) domain that are involved in anchoring VGCC complexes at presynaptic sites, a guanylate kinase-like (GK) domain with which they bind to the α-interacting domain of Cav1 and Cav2 I–II loops and a HOOK domain critical in modulating VDI of its associated VGCC (4). However, it is the N-terminus that imparts the profoundly VDI-slowing properties to β$_{2a}$ and β$_{2e}$ and thus constitutes an important functional determinant.

The N-terminal end is extensively alternatively spliced in Cavβ$_2$ (5), with canonical alternative exons 1A|B and 2A|B|C|D, giving rise to at least five different N-terminal sequences that have profound impact on the biophysical properties of associated Ca^{2+} channels (for reviews, see Refs. (2, 5–7)). It has been shown that both β$_{2a}$ and β$_{2e}$ can associate with the plasma membrane independent of binding to an α1 subunit. For β$_{2a}$, this membrane targeting is mediated by palmitoylated cysteines in its N-terminus (8) and underlies its effect on channel properties (9). β$_{2e}$ interacts with the plasma membrane through positively charged residues and hydrophobic side chains in its N-terminal sequence (10). It is this membrane anchoring by the alternatively spliced N-termini that crucially determines the VDI-slowing effect of β$_{2a}$ and β$_{2e}$ (5, 10).

Thus far, β$_{2a}$ and β$_{2e}$ have been the only two N-terminus variants described among all Cavβ isoforms to be membrane anchored. In the retina, the Ca^{2+} channel complex expressed in rod and cone photoreceptors responsible for synaptic release was thought to contain a splice variant of β$_{2a}$, termed

* For correspondence: Hartwig Seitter, hartwig.seitter@gmail.com; Alexandra Koschak, alexandra.koschak@uibk.ac.at.

β_{2X13} (11), in complex with Cav1.4-α1 and $\alpha_2\delta$-4. The β_{2X13} variant is identical to β_{2a} except for its HOOK domain, which contains short exon 7B instead of the longer exon 7A. Screening mouse retina RNA-Seq data (12), we confirmed the shorter HOOK domain with predominant splicing of exon 7B over exon 7A in β_2. However, we observed unexpected N-terminal β_2 splicing containing a novel exon, which suggested the existence of a hitherto undescribed N-terminus splice variant. Therefore, we aimed to investigate fundamental characteristics of this novel β_2 variant, including its expression inside and outside the retina, biophysical properties it imparts on Ca^{2+} channels, intrinsic membrane targeting, and the functional implications that distinguish it from the established canonical variants.

Results

RNA-based evidence for a novel splice variant of Cavβ$_2$ expressed in mammalian retina

Since RNA-Seq is one of the most powerful tools to reveal the complexity of mRNA transcripts, we screened publicly available RNA-Seq data of wildtype mouse retina (12) for alternatively spliced exons of the main Cavβ subunit isoform of the retina, β_2, using Integrative Genomics Viewer (IGV) visualization of mapped reads. In line with previous studies that found predominant expression of alternative exon 7B in human retina β_2 (11) RNA-Seq data suggested that also in mouse retina exon, 7B inclusion was predominant over inclusion of exon 7A (Fig. 1*A*, *inset*; predominance based on the numbers of splice junction–mapping reads upstream and

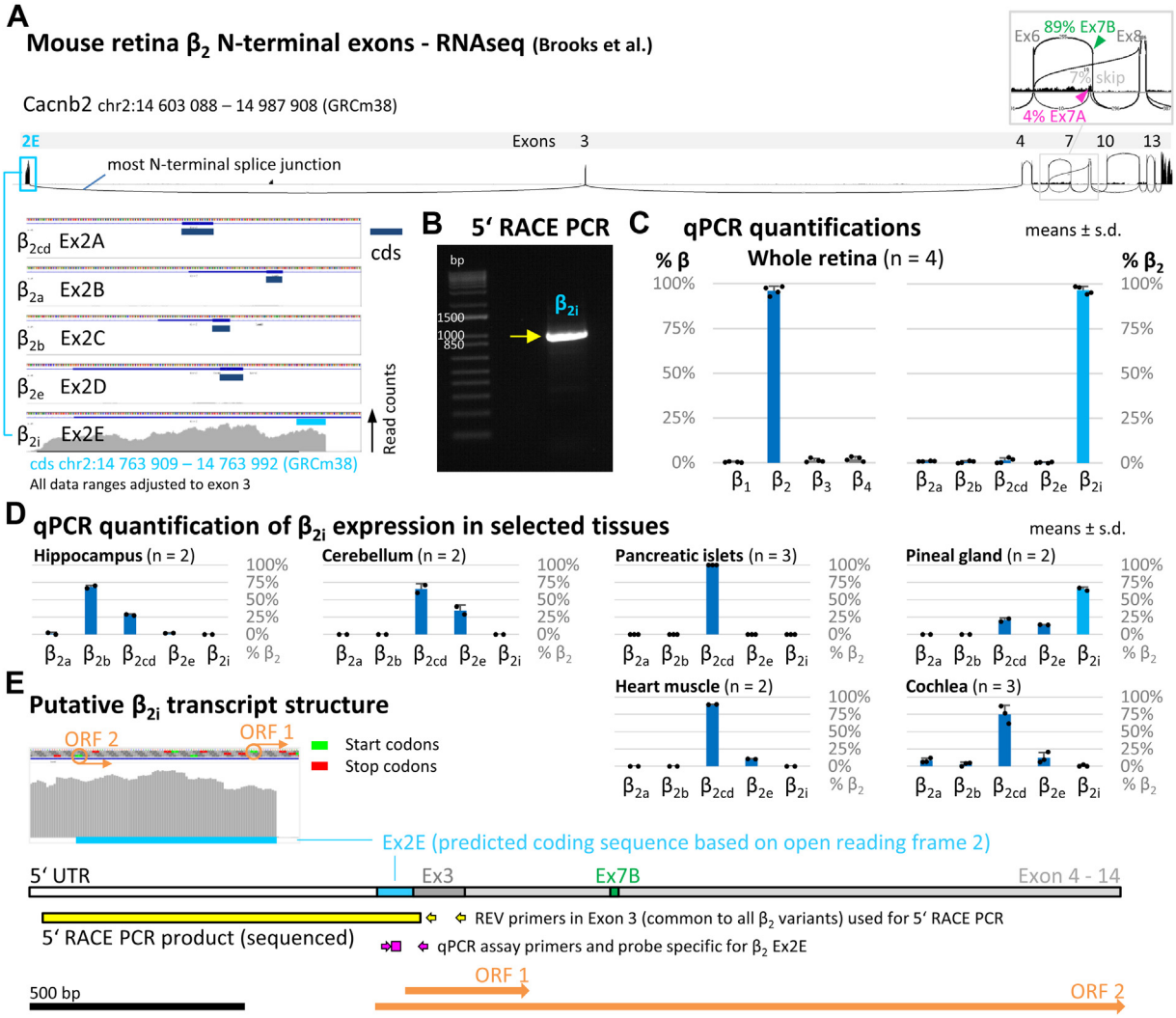

Figure 1. RNA-Seq data evidence for a novel N-terminus splice variant of Cavβ$_2$ in mouse retina. *A*, RNA-Seq data from mouse retina suggested splicing of a single β_2 N-terminus variant upstream of canonical exon 3. The lack of both splice junction–mapping reads connecting to canonical exons 2A–2D and reads mapping to these exons indicated predominant splicing of the novel putative exon, which we named exon 2E. We called the putative β_2 splice variant containing this novel exon β_{2i}. Predominant inclusion of Ex7B (89% of splice junction–mapping reads downstream of Ex6) over Ex7A was also evident. *B*, seminested 5′-RACE PCR yielded an N-terminal sequence upstream of exon 3 containing exon 2E (*arrow-marked product*, verified by sequencing). *C*, quantitative PCR (qPCR) quantification showed near-exclusive expression of the novel N-terminal sequence variant β_{2i} in mouse retina (β_{2cd} assay detects both variants). *D*, qPCR quantification revealed dominant expression of β_{2i} in pineal gland but not in a selection of other tissues. *E*, the sequence of Ex2E contains start codons for two potential ORFs. ORF 2 is in-frame with Ex3–Ex14 and thus yields a complete β_2 transcript. Based on ORF 2, we predicted the putative coding sequence of Ex2E with a long 5′-UTR. The 5′-RACE PCR product and primers used, as well as the custom qPCR assay location, are marked. RACE, rapid amplication of cDNA.

exon-mapping read counts). Similarly, exon 7B inclusion was predominant in rod and cone photoreceptors as well as rod bipolar cells (Fig. S1*A*) suggesting the same splice pattern of the β_2 HOOK region in these cell types. However, we were surprised to discover a novel alternative splice pattern at the distal N-terminus. Unexpectedly, splice junction–mapping reads at the N-terminus of β_2 did not link exon 3 (common to the known N-terminus splice variants (5)) to upstream exons of any known canonical β_2 splice variant. Instead, all reads showing splicing upstream of exon 3 mapped to a genomic region for which no protein-coding exons were annotated (Fig. 1*A*). Closer inspection of this genomic region revealed a splice donor site right after the 3′ end of the unknown sequence, but no splice junction–mapping reads further upstream, suggesting that this sequence constitutes a novel first exon of a β_2 splice variant transcript. We named this sequence exon 2E and the resulting novel Cavβ_2 subunit β_{2i}, in line with the established exons 2A to 2D of Cavβ_{2a-e} and the nomenclature of described Cavβ_2 variants (5).

In-frame translation with exon 3 was predicted to lead to an ORF with a short coding sequence (cds; location chr2: 14,763,909–14,763,992 [GRCm38/mm10]) of exon 2E (84 bp) and a long 5′-UTR. We confirmed experimentally that exon 2E constitutes the 5′-end of a transcript in mouse retina by 5′-rapid amplication of cDNA end (RACE) PCR (Fig. 1*B*) using full-length mouse retinal complementary DNA (cDNA) and amplifying the 5′ end of β_2 with primers in canonical exon 3 in a seminested approach. The PCR product was verified by sequencing and corresponded to exon 2E with a long 5′-UTR spliced to exon 3, as predicted from RNA-Seq. Quantitative real-time PCR (qPCR) analysis confirmed β_2 as the major Cavβ isoform expressed in mouse retina and showed that exon 2E defines the 5′ cds of retinal β_2 almost exclusively (Fig. 1*C*). The exclusive expression of β_{2i} held equally true when we analyzed cell type–specific RNA-Seq data of rod and cone photoreceptors as well as rod bipolar cells (Fig. S1*A*), and we could confirm the predominance of exon 2E/β_{2i} in these cell types experimentally by qPCR on fluorescence-activated cell sorting–purified cell populations (Fig. S1*B*). Thus, RNA-Seq data and our qPCR experiments provided substantial evidence that β_{2i} is the major β_2 variant in all ribbon synapse–bearing cell classes in mouse retina. Similarly, we found that the homologous sequence of exon 2E also likely predominates the N-terminus of β_2 in human, rhesus monkey, and rat retina (Fig. S2), suggesting conservation of β_{2i} as the major retinal β_2 variant in mammals (see evolutionary conservation of homologous sequences in Fig. S4). We quantified β_{2i} expression by qPCR in nonretinal tissues (pineal gland, pancreas, heart muscle, and cochlea) and brain regions (cortex, cerebellum, striatum, and hippocampus), among which only pineal gland showed substantial expression (Figs. 1*D* and S3). This suggests that β_{2i} in mouse is largely specific for retina and pineal gland, which are closely related in their gene expression patterns (13). We outlined the putative transcript structure of β_{2i} (Fig. 1*E*) with two potential ORFs (see zoom-in of RNA-Seq visualization) of which ORF 2 (in-frame with exon 3) yields a complete β_2 transcript with the short cds of exon 2E described previously and a long 5′ UTR with predominant inclusion of exon 7B.

Transcript structure and predicted protein sequence of β_{2i} show distinct N-terminus features

The overview of the exon structure and encoded domains of selected β_2 splice variants and β_{2i} (Fig. 2*A*) shows that β_{2i} has highest similarity with β_{2X13}, containing exon 7B instead of exon 7A, albeit with a different N-terminus (5). A sequence comparison of the established β_2 splice variants with the predicted N-terminal amino acid sequence of β_{2i} (Fig. 2*B*) showed that β_{2i} differs in several relevant features that determine crucial aspects of β_2 function like interaction with the plasma membrane (14). First, there are no cysteines in β_{2i}, and therefore S-palmitoylation, which is necessary for β_{2a} membrane association (3, 8, 9, 15, 16), is not expected (*dark red* in Fig. 2*B*). Moreover, the β_{2i} sequence shows only few positively charged amino acids (similar to β_{2b-d}, *gray* in Fig. 2*B*), which are required for β_{2e} membrane association (10). However, β_{2i} contains a striking accumulation of hydrophobic amino acids that are especially concentrated at the very N-terminal end (*green* in Fig. 2*B*). Thus, the β_{2i} N-terminus by far exceeds the hydrophobicity (43% of exon 2E-encoded residues belong to the most hydrophobic amino acids: ILVFW) of the N-termini of known splice variants (10–26%). The hydrophobic character is preserved in human β_{2i} (predicted from homologous sequence), which shows high overall sequence similarity with mouse β_{2i} (78% sequence identity). High evolutionary conservation of predicted β_{2i} sequence features was indeed found across mammalian and nonmammalian vertebrate species (Fig. S4) including, but not limited to, the strongly hydrophobic character.

Biophysical properties of Cav1.4 complexes with β_{2i}

We studied the basic functions of β subunits for this splice variant, namely the modulation of VGCC current properties. We recorded Ca^{2+} currents from tsA-201 cells heterologously expressing human Cav1.4 α1 together with $\alpha_2\delta$-4 and different β_2 subunits: β_{2X13}, β_{2a}, and β_{2d} in comparison to β_{2i}. We have selected these Cavβ subunits for the comparison because the membrane-associated β_{2X13} and β_{2a} have been proposed to be dominantly expressed in the retina and β_{2X13} shares inclusion of exon 7B with β_{2i}, making it the closest match only differing in the N-terminal sequence. β_{2d} served as reference for a nonmembrane-associated variant.

As shown in plots of current–voltage (I–V) relationships (Fig. 3*A* and see Table 1 for parameters), current densities of Cav1.4 complexes with β_{2i} were smaller than with β_{2d} (p = 0.004) but not significantly different from β_{2a} (p = 0.344) or β_{2X13} (p = 0.996). The activation threshold determines the range where channels begin to open and was defined as the voltage where currents reached 5% of the maximal current. Activation threshold with β_{2i} was similar as with β_{2X13}, β_{2a}, and β_{2d} (p = 0.797; p = 0.483; p = 0.222, respectively). By contrast, in the presence of β_{2i}, voltage dependence of activation properties of Cav1.4, determined by the voltage of half-maximal currents

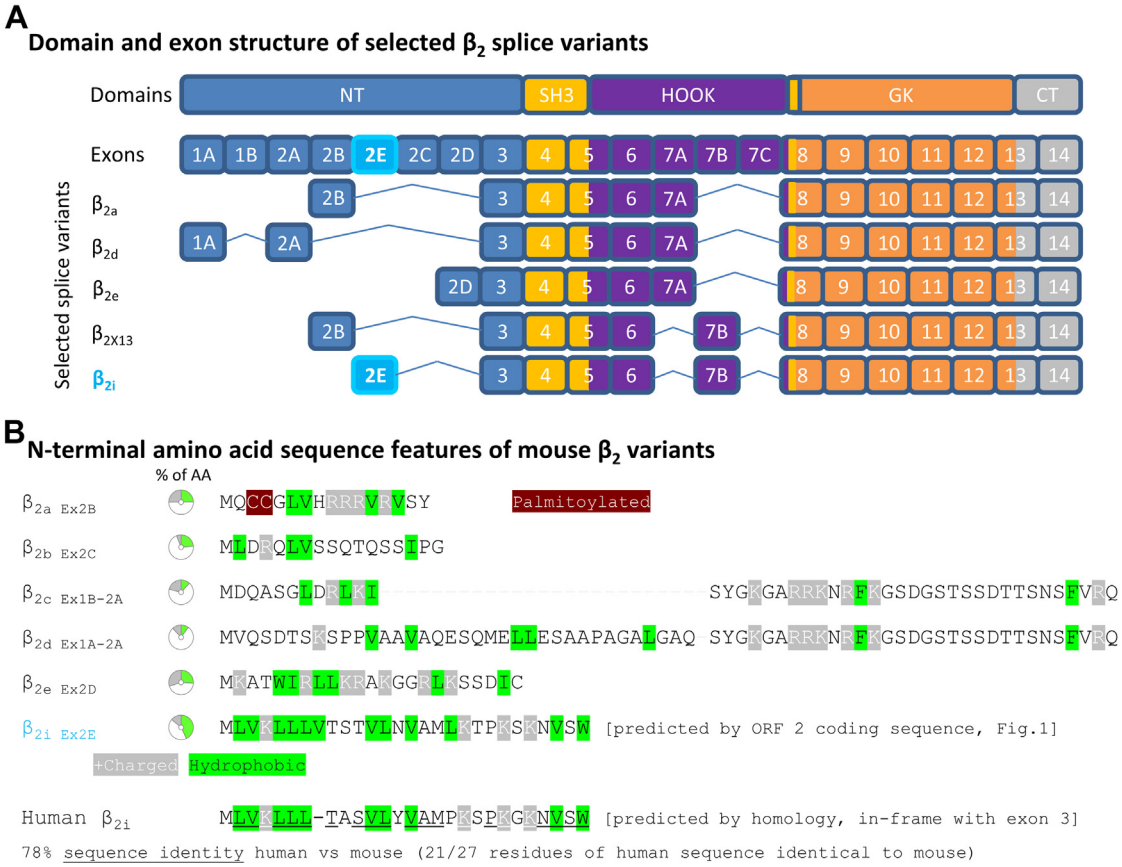

Figure 2. β$_2$ splice variant exon composition and N-terminal amino acid sequence features. *A*, comparison of selected β$_2$ splice variants and β$_{2i}$ exon composition (based on the RNA-Seq evidence of predominant exon 7B inclusion). *B*, the predicted N-terminal sequence of β$_{2i}$ contains no cysteines (see β$_{2a}$) and no accumulation of charged residues (see β$_{2e}$) but features extraordinarily high hydrophobicity (43% of residues). The predicted human β$_{2i}$ sequence (based on RNA-Seq evidence of exonic sequence and conceptual translation in-frame with exon 3) has high sequence identity to mouse β$_{2i}$, including the hydrophobic residues.

($V_{0.5}$) and maximal currents (V_{max}), was partly right-shifted in comparison to β$_{2X13}$ (p = 0.034; $V_{0.5}$ and p = 0.119; V_{max}) yet similar to β$_{2a}$ (p = 0.876; $V_{0.5}$ and p = 0.251; V_{max}) and β$_{2d}$ (p = 0.842; $V_{0.5}$ and p = 0.955; V_{max}). The statistics employed were one-way ANOVA with multiple comparisons to β$_{2i}$.

We measured Ca^{2+} current inactivation during prolonged depolarizations, for which all Cavβ$_2$ subunits supported slowly inactivating Cav1.4 currents (Fig. 3*B*). Note, that despite recording with Ca^{2+} as charge carrier, Ca^{2+}-dependent inactivation is absent in Cav1.4 (17), and thus, the current inactivation reflects only VDI properties. We measured Cav1.4 inactivation as the fractional remaining current amplitude at the end of a 5-s test pulse to V_{max}. Remaining currents were comparable between β$_{2i}$ (77.91% ± 8.01%) and β$_{2X13}$ (74.98% ± 14.60%; p = 0.877) as well as β$_{2a}$ (73.54% ± 8.31%; p = 0.668) and showed a tendency to reduced inactivation with β$_{2i}$ compared with β$_{2d}$ (66.37% ± 12.49%; p = 0.073; means ± SD; one-way ANOVA with multiple comparisons to β$_{2i}$). Thus, current inactivation properties with β$_{2i}$ were generally similar to the membrane-associated variants β$_{2X13}$ and β$_{2a}$. This biophysical characteristic could be consistent with a potential membrane association of β$_{2i}$ that might underlie slow inactivation, but differentiation in slowly inactivating Cav1.4 was limited.

Currents in Cav1.2 complexes with β$_{2i}$ are slowly inactivating

We characterized inactivation properties also with Cav1.2 with the aim of achieving a more pronounced difference in VDI between membrane-associated (β$_{2a}$ for comparison) and nonmembrane-attached (β$_{2d}$ for comparison) β$_2$ variants compared with the slowly inactivating Cav1.4. We chose Cav1.2 because it supports well-studied VDI kinetics (18, 19). We measured Ba^{2+} currents, to exclude Ca^{2+}-dependent inactivation, through Cav1.2 in complex with α$_2$δ-1 and β$_2$ variants. The I–V relationships (Fig. 4*A*, and see Table 2 for parameters) showed that current densities of Cav1.2 complexes with β$_{2i}$ were not significantly different from β$_{2d}$ (p = 0.818) or β$_{2a}$ (p = 0.812). The activation threshold with β$_{2i}$ was right-shifted compared with β$_{2a}$ (p = 0.032) but left-shifted compared with β$_{2d}$ (p = 0.009). The voltage-dependent activation properties of Cav1.2 with β$_{2i}$ were comparable in V_{max} and $V_{0.5}$ with β$_{2a}$ (p = 0.979; $V_{0.5}$ and p = 0.999; V_{max}) and β$_{2d}$ (p = 0.803; $V_{0.5}$ and p = 0.999; V_{max}).

Remaining currents at the end of 5-s pulses (Fig. 4*B*) with β$_{2i}$ (28.4% ± 8.5%; means ± SD) were lower than with membrane-associated β$_{2a}$ (41.2% ± 18.7%; p = 0.041) but significantly higher than with cytosolic β$_{2d}$ (14.7% ± 9.9%; p = 0.024). The reduced VDI in comparison to β$_{2d}$ suggested a potential membrane attachment of β$_{2i}$.

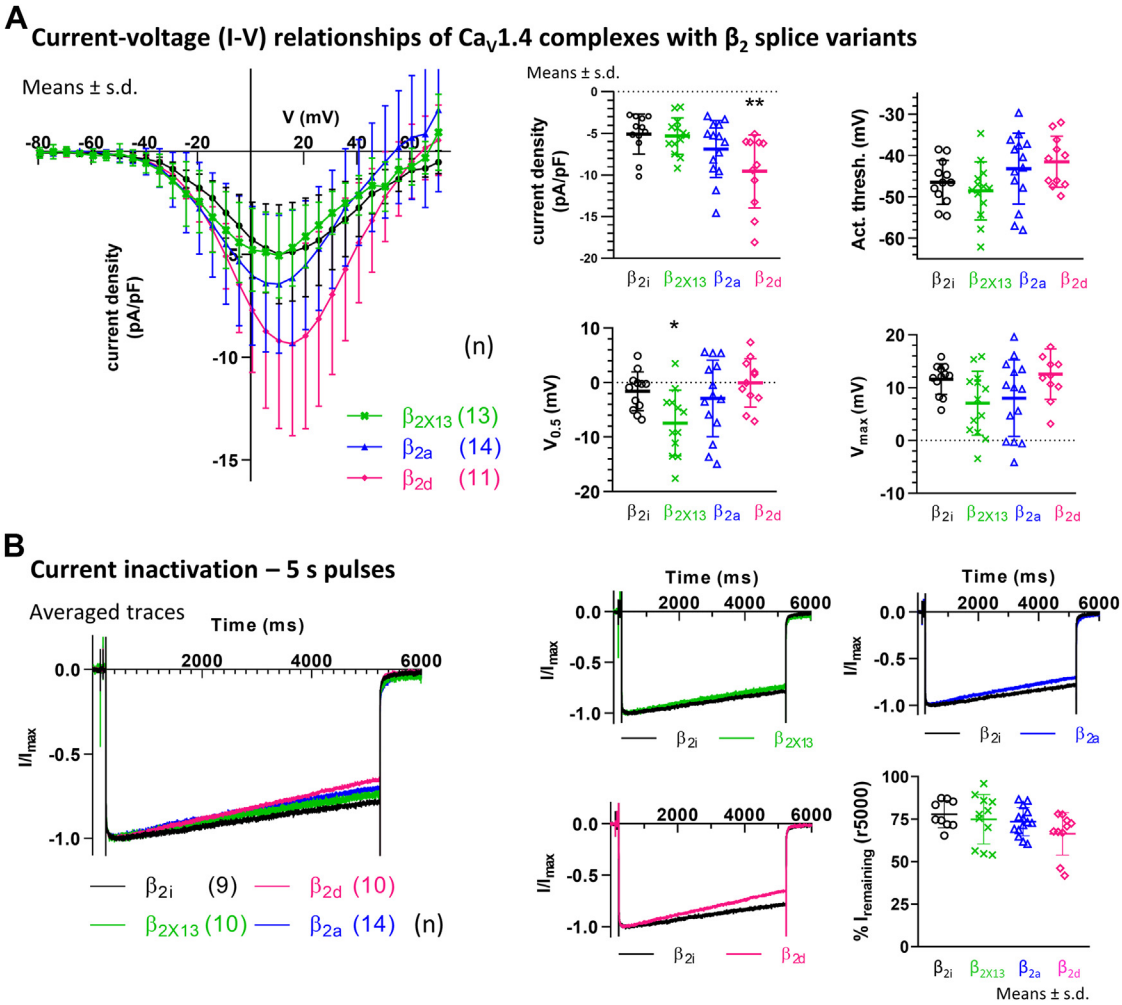

Figure 3. Electrophysiology of calcium currents in Cav1.4 complexes with β$_2$ variants. β$_2$ variants were coexpressed in tsA-201 cells together with Cav1.4 and α$_2$δ-4. Currents were recorded in 15 mM Ca^{2+}. *A*, current densities of Cav1.4 complexes with β$_{2i}$ were smaller than with β$_{2d}$ but not significantly different from β$_{2X13}$ or β$_{2a}$. The activation threshold was comparable among the variants tested. The voltage dependence ($V_{0.5}$ but not V_{max}) with β$_{2i}$ was partly *right-shifted* in comparison to β$_{2X13}$. There was no difference in the voltage dependence between β$_{2i}$ and β$_{2a}$ or β$_{2d}$ (for details, see Table 1 and text). *B*, normalized currents during a 5 s pulse to V_{max}. Current inactivation with β$_{2i}$ during the 5 s pulse was not significantly different from β$_{2X13}$ or β$_{2a}$ but showed a tendency to slower inactivation than with β$_{2d}$ (see text for details). Statistics: one-way ANOVA with multiple comparisons to β$_{2i}$.

β$_{2i}$ is membrane associated and exhibits distinct intrinsic localization properties

The functional properties that β$_{2i}$ subunits confer to Cav1.4 and Cav1.2 channel complexes were consistent with a potential membrane association of β$_{2i}$ subunits independent of the channel complex. Therefore, we tested membrane targeting of β$_{2i}$ by heterologously expressing mEmerald (mEm)-tagged β$_2$ subunits in the absence of a Cavα1 in tsA-201 cells. We assessed the subcellular localization of these tagged β$_2$ variants using the mEm fluorescence together with the plasma membrane stain CellMask (Fig. 5*A*) in live cells. Line scan analysis provided cross sections through the fluorescence intensity profiles, which revealed colocalization of mEm with the CellMask fluorescence in variants with membrane association (Fig. 5*B*).

The known membrane-anchored variants β$_{2a}$, β$_{2X13}$, and β$_{2e}$ associated with the plasma membrane, whereas β$_{2d}$ was located in the cytosol of the cells, as was unconjugated mEm that was used as control. Unconjugated mEm was also seen in the nucleus, which is common for GFP derivatives (20). By

Table 1
I–V properties of Cav1.4 with α$_2$δ-4 and different β$_2$ variants

β$_2$ variant (no. of recordings)	Current density (pA/pF)	Activation threshold (mV)	$V_{0.5}$ (mV)	V_{max} (mV)
β$_{2i}$ (12)	−5.074 ± 2.385	−46.457 ± 5.323	−1.565 ± 3.539	11.616 ± 2.913
β$_{2X13}$ (13)	−5.306 ± 2.182	−48.531 ± 7.013	−7.406 ± 6.015*	7.063 ± 6.046
β$_{2a}$ (14)	−6.880 ± 3.429	−43.134 ± 8.586	−2.885 ± 7.018	8.017 ± 7.255
β$_{2d}$ (11)	−9.555 ± 4.392**	−41.487 ± 6.164	−0.022 ± 4.455	12.575 ± 4.742

Data are presented as means ± SD. Statistics: one-way ANOVA multiple comparisons to β$_{2i}$.
Abbreviations: $V_{0.5}$, half maximal voltage of activatio; V_{max}, voltage of maximal current influx.
Significance levels of $p < 0.05$ or $p < 0.01$ are denoted by a single or double asterisk, respectively.

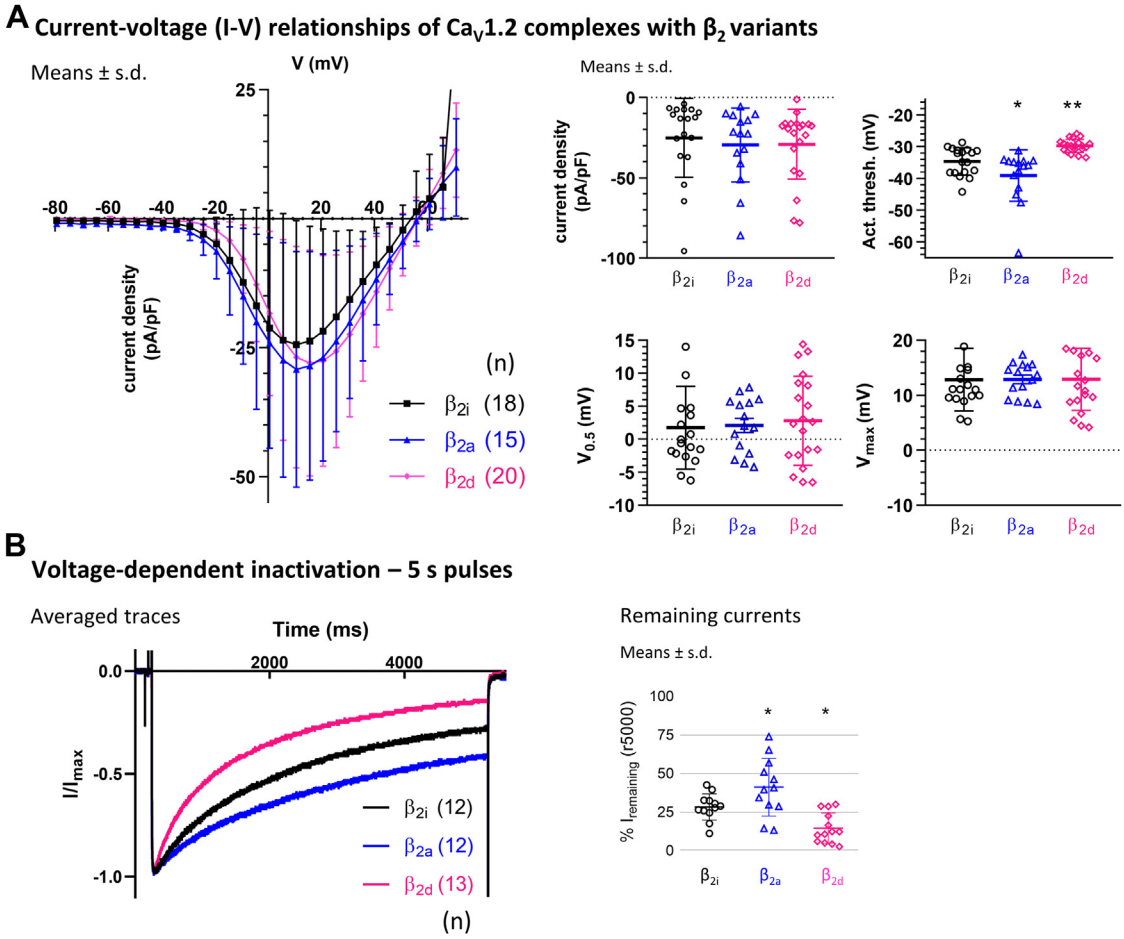

Figure 4. Electrophysiology of currents in Cav1.2 complexes with β$_2$ variants. β$_2$ variants were coexpressed in tsA-201 cells together with Cav1.2 and α$_2$δ-1. Currents were recorded in 15 mM Ba^{2+}. *A*, current densities were comparable with β$_{2i}$, β$_{2d}$, and β$_{2a}$. Activation thresholds were different from β$_{2i}$ with β$_{2d}$ (*right-shifted*) and with β$_{2a}$ (*left-shifted*), whereas voltage dependence ($V_{0.5}$ and V_{max}) was comparable throughout (for details, see Table 2 and text). *B*, normalized Ba^{2+} currents during 5 s pulses to V_{max}. Voltage-dependent inactivation with β$_{2i}$ during the 5 s pulse was faster than with β$_{2a}$ but slower than with β$_{2d}$ (see text for details). Statistics: one-way ANOVA with multiple comparisons to β$_{2i}$.

contrast, β$_{2i}$ showed subcellular distributions that differed from the other β$_2$ splice variants and could be observed in three major patterns. First, β$_{2i}$ was localized perinuclear and in a web-like manner throughout the cell volume, reminiscent of the endoplasmic reticulum (ER). Second, β$_{2i}$ accumulated in a single dense cluster within the cytoplasm. This dense intracellular accumulation was confirmed as the Golgi apparatus (Fig. 6) by coexpression of a Golgi marker (Giantin-mScarlet) with mEm-tagged β$_{2i}$ and β$_{2X13}$ or with unconjugated mEm. Accumulation of mEm fluorescence in the Golgi apparatus did not occur with β$_{2X13}$ or with mEm alone showing a dependence of the Golgi accumulation on the β$_{2i}$ N-terminus. Third, we found β$_{2i}$ in clusters overlapping with the plasma membrane marker. These clusters of β$_{2i}$ at the membrane were numerous and very commonly seen while focusing through the convex shape of the cell surface or bottom part of cells adhering to the coverslip (see example Video in supporting information). Still, for colocalization with the membrane marker, only clusters within the optical membrane cross-section (*i.e.*, perpendicular to the coverslip surface) were used. The three localization patterns were not mutually exclusive as reticular and Golgi localization often occurred in parallel with membrane colocalization. In addition, β$_{2i}$ consistently exhibited a clustered appearance as opposed to the largely homogeneous cytosolic (β$_{2d}$) or membrane-localized (*e.g.*, β$_{2X13}$) distributions of the other β$_2$ variants.

Table 2
IV properties of Cav1.2 with α$_2$δ-1 and different β$_2$ variants

β$_2$ variant (no. of recordings)	Current density (pA/pF)	Activation threshold (mV)	$V_{0.5}$ (mV)	V_{max} (mV)
β$_{2i}$ (18)	−25.15 ± 24.55	−34.62 ± 4.34	1.75 ± 6.29	12.85 ± 5.69
β$_{2a}$ (15)	−29.51 ± 22.92	−39.05 ± 8.11*	2.11 ± 4.14	12.88 ± 3.01
β$_{2d}$ (20)	−29.12 ± 19.41	−29.70 ± 2.19**	2.83 ± 6.79	12.90 ± 5.58

Data are presented as means ± SD. Statistics: one-way ANOVA multiple comparisons to β$_{2i}$.
Abbreviations: $V_{0.5}$, half maximal voltage of activation; V_{max}, voltage of maximal current influx.
Significance levels of $p < 0.05$ or $p < 0.01$ are denoted by a single or double asterisk, respectively.

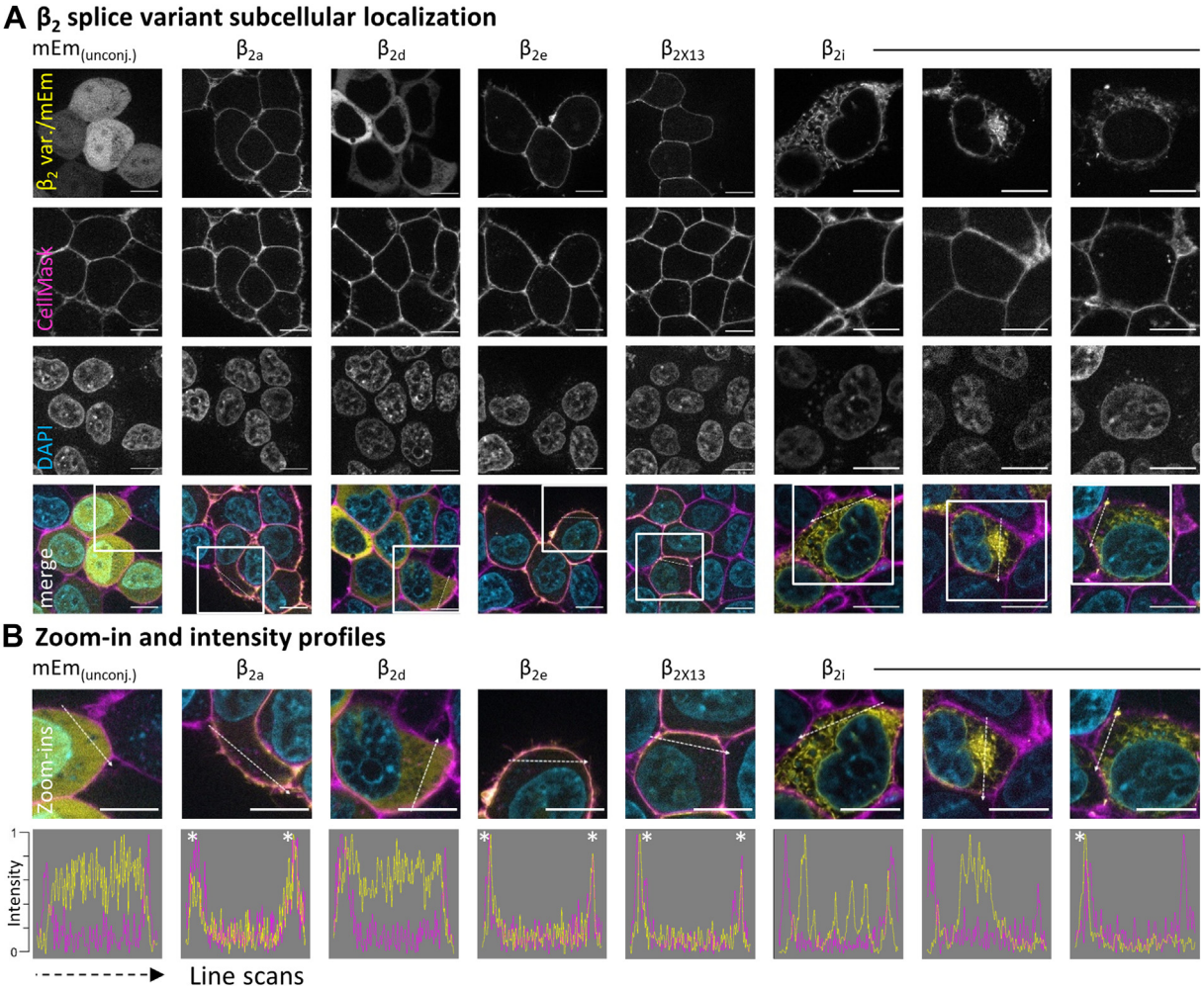

Figure 5. β$_{2i}$ subcellular localization differs from known splice variants. *A*, β$_2$ splice variants were C-terminally tagged with the fluorescent reporter mEmerald (mEm) and expressed in tsA-201 cells without Cavα1 subunits to track their intrinsic membrane association properties. The β$_2$ subunit localizations (visualized by conjugated mEm fluorescence) were overlapping with the plasma membrane marker CellMask in β$_{2a}$, β$_{2e,}$ and β$_{2X13}$, whereas β$_{2d}$ was localized mostly intracellularly, similar to unconjugated mEm. For β$_{2i,}$ we observed three patterns of localization (*left to right*): intracellular (web-like), intracellular (accumulated), and membrane colocalized. Notably, in all three patterns, the localization of β$_{2i}$ appeared clustered. *B*, zoom-ins of the regions marked above. Line scans provided intensity profiles of mEm and CellMask, highlighting the overlap of β$_2$ subunit–conjugated mEm fluorescence with the plasma membrane (marked by * in *line scans*) in β$_{2a}$, β$_{2e}$, β$_{2X13}$, and β$_{2i}$ (*right-most panel*). The scale bars represent 10 μm.

Yet, with low frequency, a more homogenous cytosolic localization of β$_{2i}$ could also be observed (1–2% of fluorescent cells). The membrane colocalization was illustrated in line scans showing overlap between CellMask fluorescence profiles and mEm (* in Fig. 5*B*), highlighting the overlay of the membrane and the β$_{2i}$ cluster in the example image. In summary, we observed a clustered localization of β$_{2i}$ from a reticular appearance through the Golgi apparatus to widespread dense clusters at the plasma membrane.

Since β$_{2i}$ showed clear membrane association, we set out to determine the impact of different amino acids within the N-terminus on the subcellular localization. As the mouse β$_{2i}$ sequence contains no cysteines or glycines as post-translational palmitoylation targets, we considered three other possibilities that might explain the membrane localization of the protein: 1—positively charged lysine residues that interact with negatively charged phospholipids (as in β$_{2e}$ (10)), 2—serine and threonine residues as potential targets for other types of post-translational modification (acylated Ser/Thr as myristoylation/palmitoylation targets, similar to β$_{2a}$ (8)), or 3—direct interaction of the highly hydrophobic N-terminus with the lipid bilayer of the plasma membrane itself.

To test the role of these three candidate mechanisms, we cloned modifications that contained alanine substitutions of the respective residues (Fig. 7*A*) and expressed them in tsA-201 cells. While the lysine modification (K>A) and serine/threonine modification (TS>A) neither altered the clustering nor the membrane localization, substitution of hydrophobic residues (LV>A) lead to a homogeneous fully cytosolic localization (Fig. 7*B*), similar to β$_{2d}$ (used as cytosolic control, with β$_{2X13}$ as membrane-associated control). For quantification of membrane colocalization, cells were imaged 48 h post-transfection, during which β$_{2i}$ membrane clusters typically grew in size, and regions of interest were selected around visually identified mEm clusters (for β$_{2i}$) or similarly sized image sections from the other variants (see example image sections in Fig. S5*A*). The degree of colocalization of the expressed β$_2$ splice variants with the plasma membrane was

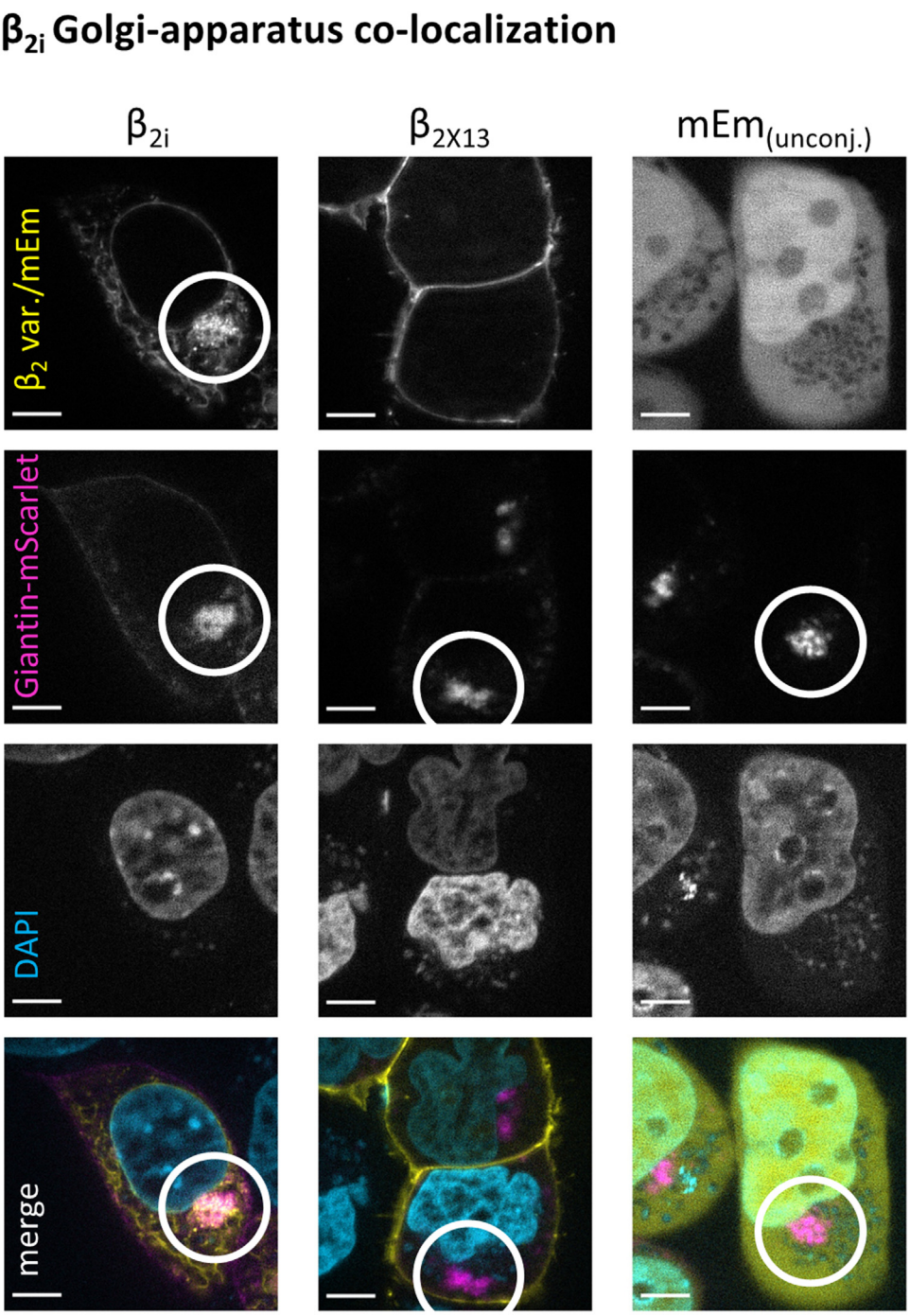

Figure 6. β$_{2i}$ accumulation in the Golgi apparatus. The intense intracellular accumulation of β$_{2i}$ colocalized with the Golgi apparatus, revealed by colabeling with a Golgi marker (cotransfected plasmid coding for Giantin-mScarlet) while clustering of mEm fluorescence at the Golgi was not observed with β$_{2X13}$ or unconjugated mEmerald. Scale bars represent 5 μm.

quantified by the Mander's coefficient (MC) of colocalization between mEm and CellMask signals (percent of mEm-positive pixels overlapping CellMask-positive pixels, thresholding example see Fig. S5*B*) for β$_{2i}$, β$_{2i}$ modifications, β$_{2d}$ and β$_{2X13}$ (Fig. 7*B*, *bottom*). β$_{2i}$ showed a high degree of membrane colocalization (MC = 0.761) similar to the β$_{2i}$ K>A and TS>A modifications (MC = 0.766; p = 0.997 and MC = 0.755; p = 0.999, respectively) and comparable to β$_{2X13}$ (MC = 0.710; p = 0.216), whereas the β$_{2i}$ 10LV>A modification exhibited a significantly reduced membrane colocalization (MC = 0.109; $p < 0.001$), close to cytosolic β$_{2d}$ (MC = 0.170; $p < 0.001$; one-way ANOVA with multiple comparisons to β$_{2i}$).

We investigated in more detail whether the number or the position of hydrophobic residues are essential for the maintenance of clustering and membrane association by cloning three additional modifications, each substituting only a subset of five hydrophobic amino acid residues. We replaced 1—the first five hydrophobic residues (5LV>A first), 2—the first five odd-numbered hydrophobic residues (5LV>A odd), or 3—the first five even-numbered hydrophobic residues (5LV>A even).

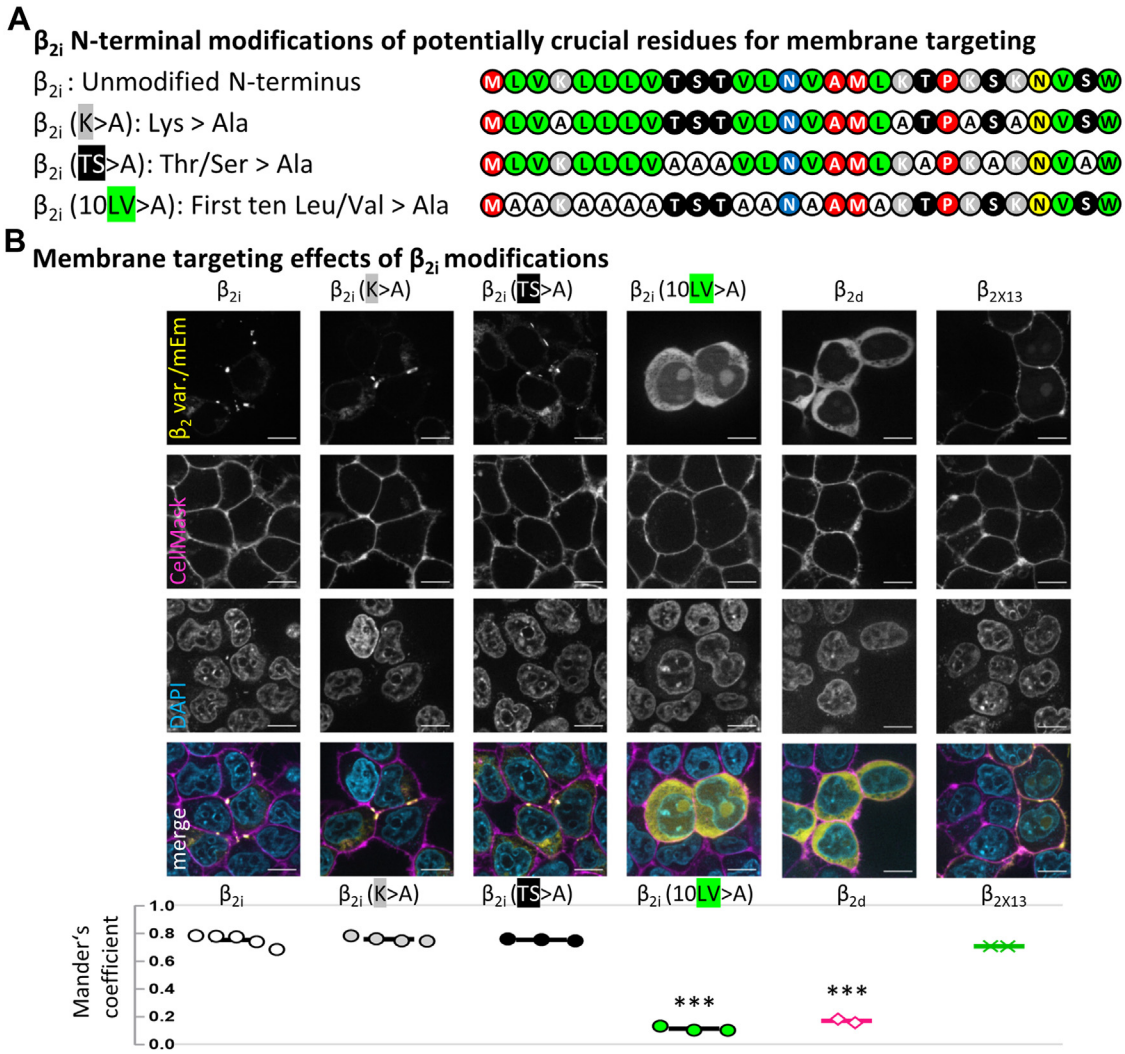

Figure 7. β$_{2i}$ membrane targeting depends on hydrophobicity. *A*, we cloned three N-terminus modifications of β$_{2i}$, replacing charges (K>A), threonines/serines (TS>A), or the first ten hydrophobic residues leucine/valine (10LV>A) by alanine substitution to identify crucial residues for the membrane-targeting property of β$_{2i}$. *B*, the K>A and TS>A modifications showed an unchanged clustered appearance and apparent membrane localization. The 10LV>A modification showed a cytosolic and homogeneous distribution, comparable to the localization of β$_{2d}$. The established membrane-localized variant β$_{2X13}$ was used for comparison. Scale bars represent 10 μm. We calculated the Mander's coefficient (fraction of mEmerald [mEm] pixels that colocalizes with CellMask pixels), showing high membrane colocalization of β$_{2i}$, the K>A and TS>A modifications, and in β$_{2X13,}$ while the LV>A modification exhibited loss of membrane colocalization with Mander's coefficient values comparable to the cytosolic β$_{2d}$ (see text for details). Statistics: one-way ANOVA with multiple comparisons to β$_{2i}$.

All three modification subsets altered the subcellular location of β$_{2i}$ in the same way as the full set of β$_{2i}$ hydrophobicity removal (10LV>A), with no cluster formation (and no reticular distribution pattern or accumulations at the Golgi apparatus) and no detectable localization at the membrane (Fig. S6). In summary, the removal of subsets of five hydrophobic residues was sufficient to abolish both cluster formation and membrane targeting of β$_{2i}$, whereas charged Lys residues and Ser/Thr residues appeared to have no role in localization or clustering.

Biophysical properties of β$_{2i}$ modifications match their membrane localization

We measured the biophysical effects of β$_{2i}$ N-terminus modifications on Ba^{2+} currents with Cav1.2 coexpressed with α$_2$δ-1 and β$_{2i}$ modifications to determine whether the membrane-localization behavior also impacts the biophysical properties. The I–V relationships (Fig. 8*A*, and see Table 3 for parameters) showed that the K>A modification did not alter current density (p = 0.990), but currents were remarkably larger with the hydrophobicity modifications 10LV>A (p = 0.009) and 5LV>A first (p = 0.007). The Cav1.2 activation threshold was not significantly shifted with the K>A (p = 0.564) but was significantly more depolarized with 10LV>A (p = 0.005) and 5LV>A first modifications (p = 0.030), akin to β$_{2d}$. The voltage dependence of activation properties of Cav1.2 with β$_{2i}$, on the other hand, were comparable in $V_{0.5}$ and V_{max} with the K>A (p = 0.115; $V_{0.5}$ and p = 0. 219; V_{max}), 10LV>A (p = 0.300; $V_{0.5}$ and p = 0. 398; V_{max}), and 5LV>A first modifications (p = 0.929; $V_{0.5}$ and p = 0. 933; V_{max}).

VDI was measured as the remaining current at the end of 5 s pulses to V_{max} (Fig. 8*B*). Compared with β$_{2i}$ remaining

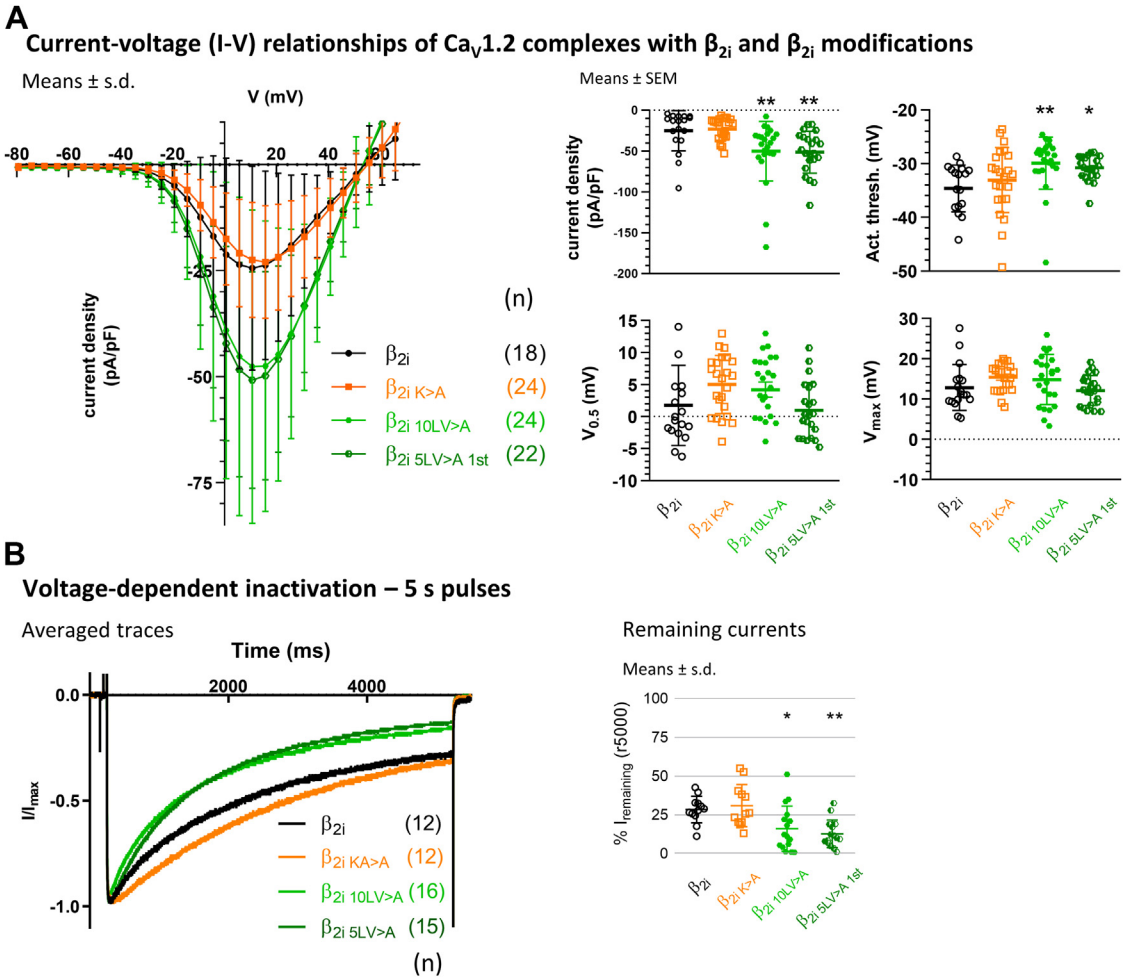

Figure 8. Electrophysiology of currents in Cav1.2 complexes with β$_{2i}$ modifications. β$_{2i}$ modifications were coexpressed in tSA-201 cells together with Cav1.2 and α$_2$δ-1. Currents were recorded in 15 mM Ba^{2+}. *A*, the K>A modification did not change current density compared with unmodified β$_{2i,}$ but current densities of the hydrophobicity modifications 10LV>A and 5LV>A first were much larger. Activation thresholds were *right-shifted* from unmodified β$_{2i}$ with the hydrophobicity modifications, whereas voltage dependence ($V_{0.5}$ and V_{max}) was comparable throughout (see Table 3 and text for details). *B*, normalized Ba^{2+} currents during 5 s pulses to V_{max}. Voltage-dependent inactivation with β$_{2i}$ during the 5 s pulse was unchanged in the K>A modification, but the hydrophobicity modifications 10LV>A and 5LV>A first showed significantly faster inactivation, as expected for a loss of membrane association (see text for details). Statistics: one-way ANOVA with multiple comparisons to β$_{2i}$.

currents (28.4% ± 8.5%; means ± SD), the K>A modification had an unchanged inactivation (30.9% ± 13.6%; p = 0.912), whereas remaining currents with 10LV>A (16.1% ± 14.5%; p = 0.023) and 5LV>A first modifications (12.8% ± 8.9%; p = 0.004) were significantly lower. In summary, we found comparable inactivation for β$_{2i}$ and the β$_{2i}$ K>A modification, whereas the β$_{2i}$ 10LV>A and β$_{2i}$ 5LV>A first modifications exhibited significantly increased inactivation, reminiscent of cytosolic β$_{2d}$ (Fig. 4). Thus, the biophysical properties matched the loss of membrane localization by the hydrophobicity modifications.

Structural investigation elucidates potential framework for β$_{2i}$ N-terminus membrane association

We sought to investigate the N-terminus on a structural level to get further insights into the potential molecular mode of action. However, a detailed survey of available β$_2$ structures from different species revealed that none of them contained

Table 3
IV properties of Cav1.2 with α$_2$δ-1 and β$_{2i}$ modifications

β$_{2i}$ modification (no. of recordings)	Current density (pA/pF)	Activation threshold (mV)	$V_{0.5}$ (mV)	V_{max} (mV)
β$_{2i}$ unmodified (18)	−25.15 ± 24.55	−34.62 ± 4.34	1.75 ± 6.29	12.85 ± 5.69
β$_{2i}$ K>A (24)	−23.21 ± 13.38	−33.08 ± 6.03	5.04 ± 4.54	15.40 ± 3.37
β$_{2i}$ 10LV>A (24)	−50.06 ± 36.36**	−29.92 ± 4.85**	4.21 ± 5.75	14.85 ± 6.21
β$_{2i}$ 5LV>A (22)	−51.45 ± 25.53**	−30.80 ± 2.29*	0.97 ± 4.36	12.13 ± 3.73

Data are presented as means ± SD. Statistics: one-way ANOVA multiple comparisons to unmodified β$_{2i}$.
Abbreviations: $V_{0.5,}$ half maximal voltage of activation; V_{max}, voltage of maximal current influx.
Significance levels of $p < 0.05$ or $p < 0.01$ are denoted by a single or double asterisk, respectively.

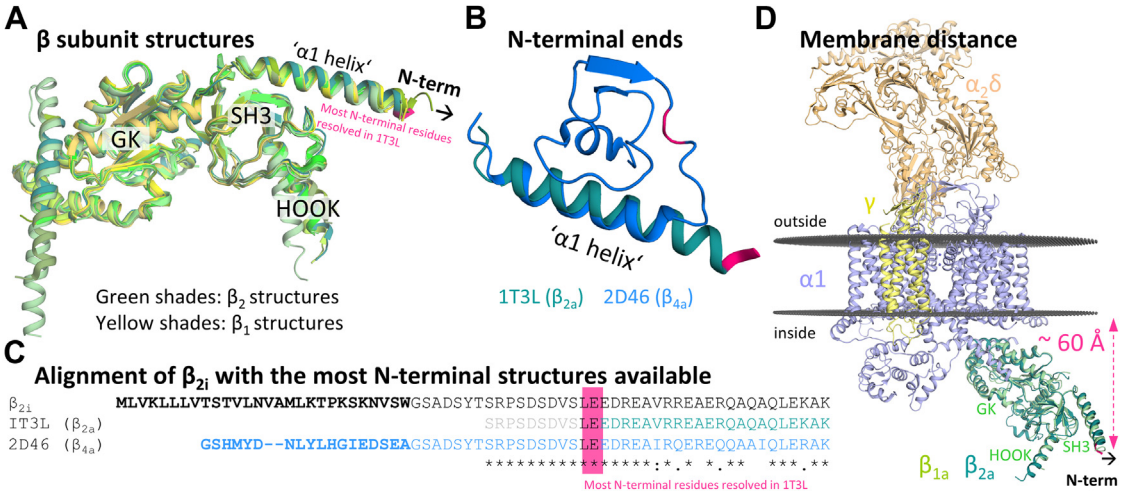

Figure 9. Structural analysis. *A*, alignment of available β$_2$ (*green shades*, Protein Data Bank [PDB] entries: 1T0H, 1T0J (21), 1T3L, 1T3S (26), 3JBR (29), 4DEX, 4DEY (67), 5V2P, and 5V2Q (67)) and full-length β$_1$ (*yellow shades*, PDB entries: 6JPA and 6JPB (24)) structures revealed missing N-termini upstream of the first α-helix (called "α1 helix") throughout. *B*, in the structure alignment of rabbit β$_{2a}$ (*green*, PDB entry: 1T3L (26)) and human β$_{4a}$ (*blue*, PDB entry: 2D46 (27)), the "α1 helix" structure is partly conserved but shorter in the β$_{4a}$ structure (see homologous residues LE in *magenta*). *C*, sequence alignment of the mouse β$_{2i}$ splice variant with rabbit β$_{2a}$ (PDB entry: 1T3L (26)) and human β$_{4a}$ (PDB entry: 2D46 (27)) constructs. Nonconserved parts in *bold*, nonresolved parts in the 1T3L structure in *light gray*. *D*, membrane-embedded Cav1.1 (α1, *violet*) in complex with auxiliary subunits β$_1$ (*light green*), α$_2$δ (*orange*), and γ (*yellow*, PDB entry: 6JPA (24)) was aligned to rabbit β$_{2a}$ (*dark green*, PDB entry: 1T3L (26)) and revealed a distance from the most N-terminal residues to the inner leaf of the membrane (*gray disc*) of ∼60 Å. For reference, the most N-terminal residues still resolved in the rabbit β$_{2a}$ structure (PDB entry: 1T3L (26)) are highlighted in *magenta* in all panels.

the N-terminus (Fig. 9*A*). This was due to the fact that the first residues were deleted in the constructs used for structure elucidation because of solubility issues (21), and in addition, the N-termini of β subunits were generally considered an intrinsically disordered region (22, 23). Similarly, in experimental complexes of the related β$_1$ isoform where full-length proteins were used for structure generation, the N-terminus remains unresolved (Fig. 9*A*) (24, 25). In Figure 6, the most N-terminal residues resolved in the rabbit β$_{2a}$ structure (Protein Data Bank [PDB] entry: 1T3L (26)) LE$_{33–34}$ were highlighted in *magenta* for reference. The only structural insights available of more N-terminal residues were provided by an NMR structure of the human β$_{4a}$ subunit (PDB entry: 2D46 (27)), which was solved under low temperature conditions to reduce protein motion. Compared with the partially resolved N-terminus of β$_{2a}$, a part of the β$_{4a}$ structure shows a shorter "α1 helix" and the homologous residues of this part (LEEDREAI in β$_{4a}$) exhibit a loop conformation instead (Fig. 9, *B* and *C*). Please note that the mouse β$_{2i}$ N-terminus shows no homology in the alignment with the human β$_{4a}$ N-terminus upstream of the highly conserved sequence region (upstream of GSADSYT) and is ten amino acids longer (Fig. 9*C*). Taken together, this indicates that the N-termini of β subunits are highly flexible and thus intrinsically difficult to resolve. Given the key role of β subunit variant N-termini in membrane anchorage, we next investigated the approximate spatial orientation of the N-terminus in relation to the membrane. For this purpose, we aligned the membrane-embedded rabbit Cav1.1 in complex with the auxiliary β$_{1a}$, γ, and α$_2$δ subunits (PDB entry: 6JPA (24)), which we downloaded from the Orientations of Proteins in Membranes database (28) (https://opm.phar.umich.edu/), to the reference rabbit β$_{2a}$ structure (PDB entry: 1T3L (26)) (Fig. 9*D*). We chose to use rabbit Cav1.1 in complex with β$_{1a}$ for a new alignment of β$_2$ because the location and orientation of the β subunit was much more reliable in this structure than in the previous published structure where β$_2$ was docked as a rigid body on a less well-resolved β$_{1a}$ (29). Our analysis suggests that the 44 most N-terminal residues of the β$_{2i}$ subunit, upstream of the resolved reference rabbit β$_{2a}$ structure (compare Fig. 9*C*), would need to span ∼ 60 Å to contact the membrane. In the absence of a solved structure, more substantial insights into potential mechanisms that underlie the described characteristics of β$_{2i}$ were not achievable. Structure prediction tools (including AlphaFold2 (30)) suggested a potential alpha helical conformation at the novel N-terminus (Fig. S7) with a roughly 70 Å-long intrinsically disordered loop connecting this helix to the conserved "α1 helix."

Discussion

Transcript

We introduced β$_{2i}$ here as a novel Cavβ$_2$ splice variant for which we provided ample and consistent experimental evidence of its exon composition, splicing pattern, and expression. While there has been no clear recognition in the literature of the existence and nature of the novel N-terminus splice variant we describe here, there have been some evidence and annotated sequences published that correspond to β$_{2i}$. In a recent publication, alternative transcript start sites specific to mouse rod photoreceptors were mapped based on chromatin signatures that revealed a novel start site for β$_2$. This novel start site is indeed localized at the β$_{2i}$ N-terminus, which was confirmed by PCR using primers in the 5′UTR of β$_{2i}$ and exon 3 in the study (31). The Ensembl database (https://www.ensembl.org) also contains a mouse *Cacnb2* transcript variant (classified as nonprotein-coding) that is composed of

the 5′UTR + exon 2E of β_{2i} spliced to canonical exons 3 to 5 (incomplete transcript), thus containing the exon 2E–exon 3 splice junction we described here (Ensembl transcript Cacnb2-205; ENSMUST00000137746.8). The Ensembl entry cites two sources of supporting information from high-throughput sequencing studies (RIKEN, ENA accession no.: AK044560.1; National Institutes of Health, ENA accession no.: BQ951456.1; https://www.ebi.ac.uk/ena/), which both used cDNA generated from mouse retina tissue samples. Thus, the pre-existing evidence for β_{2i} variant expression originated in mouse retina.

National Center for Biotechnology Information (NCBI, https://www.ncbi.nlm.nih.gov/genbank/) also contains entries corresponding to β_{2i}, based on early whole genome shotgun sequencing data from both mouse (β_2 isoform CRA_d; GenBank accession no.: EDL08070.1; conceptual translation, partial sequence/β_2 isoform X5; GenBank accession no.: XM_036157788; predicted by automated computational analysis) and human (β_2 isoform CRA_b; GenBank accession no.: EAW86194.1; conceptual translation). So, while there is prior evidence that correctly identified the alternative transcript start site or determined the splicing of exon 2E with exon 3, this has not been followed by description and recognition of this transcript as a verified alternative N-terminus variant with respective annotation.

β_{2i} seems to have a rather tissue-selective expression pattern compared with the canonical N-terminus variants, with predominance in the retina (both mouse and human) and pineal gland (which generally has a similar transcriptome as the retina) and otherwise no detectable expression in a number of other tissues that prominently feature β_2 with a variety of the canonical variants. This might suggest a special role for β_{2i} in the retina within ribbon synapse–bearing cell classes where we confirmed its predominant expression. Of note, there was no exon 2E expression detectable in whole cochlea cDNA, and thus, hair cell ribbon synapses might not contain Ca^{2+} channel complexes with β_{2i} although this should be investigated in more detail with a focus on hair cells. Expression outside the retina context could be informative as a narrow retina-selective expression pattern might be related to a distinct functional feature of β_{2i} compared with the more widespread expression of the established variants.

In addition to the novel N-terminus, β_2 in the retina also predominantly contains the alternatively spliced exon 7B coding for a part of the HOOK domain, evident from the RNA-Seq data from whole retina as well as the cell type–specific data from rods, cones, and rod bipolar cells. A previous report determined the predominant splicing of exon 7B over 7A in human retina Cavβ$_2$ (11), with an average 93.5% exon 7B inclusion *versus* 6.5% exon 7A. These numbers are close to the ratio of splice junction–mapping reads we observed for the splice junctions connecting exon 7A *versus* 7B to upstream or downstream exons. While the percentage of exon 7B inclusion from RNA-Seq data we present here has to be taken with a grain of salt, as quantifications based on few splice junctions are inherently variable, we consider this sufficient confirmation that also in mouse retina exon 7B inclusion strongly predominates in retinal Cavβ$_2$ transcripts and, hence, the predominant N-terminal exon 2E at large combines with exon 7B to form splice variant β_{2i}. Direct confirmation of the cosplicing of exon 2E with exon 7B within the same transcript is given by our cloning of the β_{2i} cDNA sequence from exon 2E down to exon 10, including exon 7B. While being nonquantitative, this confirms the principal existence of exons 2E and 7B within the same transcript.

Primary protein sequence

The predicted cds of the β_{2i} N-terminus contains two methionines, and translation initiation from the second methionine inside the predicted sequence cannot be excluded. Both potential start codons have a similarly weak Kozak sequence context (32) but evolutionary conservation is very high upstream of the second methionine, including full conservation of the first methionine, making the first in-frame methionine the likely translation start site. This notion has some support by the fact that our modifications of both the first five (5LV>A first) and the first five odd (5LV>A odd) hydrophobic residues fully changed β_{2i} localization. Protein translation from the second methionine in these modifications would have an unchanged sequence and show unaltered localization, which we did not observe. Aside from the most apparent feature unique to the β_{2i} N-terminus, its extraordinary hydrophobicity, the evolutionary comparison of predicted β_{2i} homologs highlights also other structural features that are highly conserved. Among those are not only the lysines (charges) and the serines/threonines, which we examined here, but also a polar residue, a putative glycosylation site, a glycine residue, and some alanine/methionine/proline residues (also on the hydrophobic spectrum). The degree of conservation suggests the relevance of these structural features beyond the hydrophobicity we focused on here and thus are also potential targets for further studies.

Beyond the high similarity among predicted β_{2i} orthologs, we found no other proteins with a strong homology to the N-terminal sequence. The most similar non-β subunit proteins revealed by a protein BLAST search (see Fig. S4*B* and supporting information for details) were bacterial transporters of the major facilitator superfamily proton symporters and ABC transporters (33). These protein families are generally flagged as integral plasma membrane proteins with multiple transmembrane domains, but structures of the homologous sequences are not available. With the limited sequence similarity of these bacterial proteins, however, knowledge about their structure would also not allow to extrapolate directly to β_{2i} to gain reliable structural insights.

Biophysics

We hypothesized that the hydrophobic nature of the β_{2i} N-terminus might support membrane interaction and thus, we compared the biophysical properties of Cav1.4 or Cav1.2 complexes with β_{2i} with the most closely related member of the β_2 family that associates with the membrane, β_{2X13}, and its closest relative β_{2a}, in comparison to cytosolic β_{2d}. The low macroscopic Ca^{2+} current density of Cav1.4 complexes with

β_{2i} was in line with the two membrane-targeting variants β_{2X13} and β_{2a}, whereas Ba^{2+} currents in Cav1.2 were no different with β_{2i} than with either β_{2a} or β_{2d}. Besides direct effects that could account for the small currents, like reduced trafficking, lower open probability or single-channel conductance, expression of membrane-targeting variants also could favor survival of cells with smaller currents with Cav1.4 because of Ca^{2+} overload caused by more slowly inactivating channels. It has been reported that β_{2a} confers increased open probability to heart ventricular myocyte L-type channels (34) and heterologously expressed Cav1.2 (35) (with unchanged single-channel conductance) leading to increased current densities. As we do not see larger current densities with β_{2a}, a reduced survival of cells with larger noninactivating currents may curtail currents with β_{2a} and perhaps also β_{2i}. Yet, effects of β_{2i} on open probability cannot be clearly deduced from macroscopic currents and should be determined with single-channel recordings.

All Cavβ subunits shift the voltage dependence of activation to more negative potentials (see Ref. (2)for overview), and β_{2i} showed only minor differences from the other variants tested. Voltage dependence of activation was shifted less in the hyperpolarized direction with β_{2i} compared with β_{2X13} with Cav1.4 and showed a less hyperpolarized activation threshold compared with β_{2a} with Cav1.2. Thus, voltage dependence of activation was overall comparable across Cavβ_2 variants tested here.

Support of slow current inactivation is the hallmark of membrane-anchored Cavβ_2 variants, most prominently in β_{2a} and β_{2e}, where they show pronounced remaining currents during prolonged depolarizing steps (14). The Cav1.4 current inactivation properties with β_{2i} were in line with the membrane-targeting variants, but showing only a tendency toward slower inactivation compared with β_{2d} after 5 s. Cav1.4 itself already supports slowly inactivating currents (17) and, possibly, therefore we did not observe differences in the inactivation kinetics imposed by the Cavβ_2 variants we measured, unlike those seen with other α1 isoforms (3, 36). In line with this notion, the effect of β_{2i} on slowing inactivation with Cav1.2 was indeed consistent with membrane association. The dependence on membrane attachment is further supported by our measurements of VDI of β_{2i} and β_{2i} modifications in complex with Cav1.2. We showed slow inactivation for unmodified β_{2i} and the K>A modification and increased inactivation for the hydrophobicity modifications 5LV>A first and 10LV>A, consistent with the membrane localization of β_{2i} and β_{2i} K>A and the cytosolic localization of the LV>A modifications.

The other factor to consider in functional aspects of β_{2i} is the alternatively spliced HOOK region. Among the established Cavβ_2 variants, only β_{2X13} and β_{2h} (same N-terminus as β_{2d} (5)) contain exon 7B, whereas the other variants express exon 7A. The shorter HOOK domains encoded by exon 7B (and its homologs that predominate in all other β isoforms) have been shown to contribute to increased inactivation (37), an effect also reported from Cav1.4 in complex with $\alpha_2\delta$-4 and β_{2X13} (11). In our experiments, we did not see this difference in inactivation between β_{2a} and β_{2X13}, possibly because of the Cav1.4 variant we used, which contains a shorter exon 9 (38) and consequently a shorter intracellular I–II loop where the β binding site, the α-interacting domain, is located. The shorter loop might prevent the additive effect of the longer HOOK domain of β_{2a} on slowing inactivation further compared with β_{2X13}. The increased inactivation with Cav1.2 and β_{2i} *versus* β_{2a} is further evidence that the shorter HOOK domain of β_{2i} curtails the slowing effect that membrane attachment has on inactivation. Thus, inactivation properties of β_{2i} might resemble most those with β_{2X13} (both having shorter HOOK domains), that is, current inactivation with β_{2i} likely is slowed down to a lesser extent than it could be with an exon 7A-encoded longer HOOK domain. Contrary to the commonly held notion that properties of retinal Cav1.4 complexes are tuned to the slowest possible current inactivation, this would rather suggest that a certain degree of inactivation of the Ca^{2+} current is indeed of functional relevance.

Subcellular localization

The experiments with fluorescently tagged Cavβ_2 variants revealed a surprising intrinsic localization behavior of β_{2i}. The localization of β_{2i} did not match any of the known variants tested, which were either diffuse cytosolic (β_{2d}) or diffuse membrane-associated (β_{2a}, $\beta_{2e,}$ and β_{2X13}) as shown previously (14). The localization of β_{2i} appeared neither freely cytosolic nor diffuse but generally inhomogeneous. The perinuclear to web-like localization we observed most likely revealed β_{2i} within the ER. Furthermore, β_{2i} accumulated strongly to the Golgi apparatus, presenting there as dense clusters, and finally also localized in a clustered fashion at the plasma membrane.

In principle, it would be conceivable that the β_{2i} N-terminus retains an interaction with the ER membrane at ER/plasma membrane junctions. However, in the heterologous expression without a Ca^{2+} channel, this would require a dual interaction of the N-terminus with both membranes to result in the plasma membrane localization we observed. In its native environment, for example, the photoreceptor terminal, β_{2i} is unlikely to maintain both ER and plasma membrane interactions, as its binding partner Cav1.4 is strictly localized to synaptic ribbons, whereas the ER is more diffusely distributed within the terminals, too distal from ribbon structures to allow Cav1.4-bound β_{2i} to interact (39, 40).

Curiously, we did not observe a similar labeling of putative ER or Golgi for β_{2a} even at earlier time points post-transfection, though it should pass through the same trafficking pathways to reach the plasma membrane. Conversely, we still observed reticular and Golgi labeling at later time points with $\beta_{2i,}$ whereas the membrane-localized clusters had grown further in size. In principle, this could be caused by a delayed forward trafficking of β_{2i}, for example, through ER- and/or Golgi-retention signals, but a delay in trafficking does not explain the clustered appearance on the membrane. While clusters of β_{2i} in the transport pathway could for example be defined by dense packing during transport, a traffic delay in itself would not lead to clustering on the membrane. The other

membrane-localized Cavβ$_2$ variants did not start out as clusters that eventually filled up the membrane homogeneously but exhibited a diffuse membrane labeling also at earlier time points post-transfection.

The clustered appearance of β_{2i} might be dependent on intermolecular interactions. While oligomerization is a known feature of Cavβ proteins, the clustering of β_{2i} was clearly distinct also from β_{2X13} from which it differs only in the N-terminus. Yet, oligomerization of Cavβ subunits is thus far attributed to homodimerization *via* their SH3 domains (41) or to homo-oligomerization and hetero-oligomerization *via* their GK domains (42) with both domains also underlying intramolecular interactions (23). As β_{2i} and β_{2X13} are identical except for the very N-terminus, the clustered appearance of β_{2i} cannot be attributed to one of these known mechanisms. Oligomerization or clustering by direct interactions of the N-terminus has not been described for Cavβ subunits and, if indeed the case for β_{2i}, would be a distinguishing feature.

An interesting point is also the potential interaction with other proteins. At present, the involvement of the Cavβ N-terminus in protein–protein interactions is an open question. Previously identified interactions of Cavβ subunits do not depend on the N-terminus. Small GTPases like RGK proteins or Rab proteins for example interact with Cavβ SH3/HOOK/GK domains either directly (40) or indirectly (43) *via* Rab3-interacting molecule proteins, and thus do not depend on the N-terminus of Cavβ subunits. Nonetheless, it will be an important avenue to explore whether the Cavβ N-terminus has roles beyond regulating intrinsic properties like membrane attachment.

For now, it is unclear which mechanism governs clustering of β_{2i} as is the mechanism by which membrane targeting is achieved, besides the apparent requirement of hydrophobic residues at the N-terminus for both properties. We cannot rule out that, for example, clustering depends on prior membrane targeting. Generally, proteins that interact with the membrane are either integral/intrinsic (*trans*-)membrane proteins that stably integrate with the membrane or peripheral/extrinsic membrane proteins that can interact more transiently with spatial or temporal precision (see Ref. (44) for an overview). While the former require a long stretch of hydrophobic residues to span the membrane, often in the form of an α helix, membrane interaction of the latter can rely on four prototypical arrangements (44): 1—electrostatic interactions (as β_{2e}), 2—lipidation (as β_{2a}), 3—insertion of a hydrophobic stretch into the membrane, or 4—an amphipathic α helix parallel to the membrane surface (or, more generally, hydrophobic protrusions (45)). Hydrophobic residues therefore play important roles in several of these membrane interaction paradigms, proposing several possibilities for β_{2i} membrane attachment with mechanisms based on hydrophobic characteristics.

Structure considerations

To elucidate the mechanism(s) behind membrane targeting and clustering, structure information about the N-terminus of β_{2i} would be highly beneficial. However, the N-terminus is missing in most available experimentally determined structures (X-ray, cryo-EM) of any β subunit variant and thereby suggests a general challenge in resolving the most N-terminal structures. Possibly, it is the disordered and flexible nature of at least part of the N-terminal ends of β subunits that precluded the N-termini from structural resolution in published structures. In fact, only the β_{4a} NMR structure (PDB entry: 2D46) contains a complete N-terminus, but this structure had to be resolved under special conditions, and it diverges on the length of the strongly conserved "α1 helix." The lack of N-terminus structural information would be consistent with a disordered loop, as suggested by the AlphaFold2 structure prediction. A disordered and flexible loop as part of the N-termini of β_2 variants could be behind the lack of experimentally determined structures because the predicted loop is formed in part by a sequence that is common to all β_2 splice variants (GSAD…DSDV, upstream of the "α1 helix"), and thus a loop structure might be a common feature of the β_2 N-terminus. Based on the AlphaFold2 loop structure suggestion, the β_{2i} N-terminus could at least potentially span the distance to the plasma membrane, enabling a membrane attachment. Our findings provide a basis for future studies to decipher the role of the β_{2i} N terminus, regarding (i) the structure of the potential loop and (ii) the membrane interaction—by a potential α helix as suggested by AlphaFold2, with hydrophobic protrusions, as a partial insertion or a full transmembrane segment.

Concluding remarks

We identified a novel splice variant of the already diverse Cavβ$_2$ N-terminus. While association of β_{2i} with the plasma membrane itself is not a novel feature, the propensity for clustering and its dependence on hydrophobic residues is distinct. As the biophysical properties of Ca^{2+} channels in complex with β_{2i} resemble those of other membrane-associated variants, other features of this variant might be more relevant for its dominant role in the retina. Identifying the mechanisms behind clustering and membrane targeting of β_{2i} could provide new insights into Ca^{2+} channel regulation in retinal ribbon synapse organization and also help closing the gap in understanding the functional roles of the large diversity of β_2 N-terminus splice variants.

Experimental procedures

RNA-Seq

We used publicly available RNA-Seq data from National Center for Biotechnology Information Gene Expression Omnibus (GEO; https://www.ncbi.nlm.nih.gov/geo/) to screen for gene expression and alternatively spliced exons. We analyzed data from mouse total retina (bulk RNA-Seq of whole retina, GEO accession GSE33141 [SRR358714–SRR358716], postnatal day 21 C57BL6 wildtype retina, (12)).

Raw FASTQ files were downloaded from GEO with the fastq-dump module of the SRA tools. Quality control of the FASTQ files was performed with fastqc and trimming, where

necessary, was performed with trimmomatic (46). The alignment of reads was done using STAR (47), with GENECODE's GRCm38 (vM21) primary assembly FASTA file. Assignment of reads to features was performed with featureCounts (48), using GENECODE's vM21 primary assembly annotation GTF file. Visualization of the reads mapping to the reference genome (mm10/GRCm38 – vM21) was performed using Broad Institute's IGV (49). All samples of a dataset were pooled for viewing in a single track, and data were displayed as Sashimi plots for visualization of splice junction mapping reads. Software versions used: Python 3.7.1, fastq-dump 2.9.4, FASTQC 0.11.8, trimmomatic 0.39, STAR 2.7.1a, featureCounts 1.6.1, R 3.6.1, and IGV 2.4.5.

Mouse tissue sample preparations

Experimental procedures were designed to minimize animal suffering and the number of used animals and approved by the national ethical committee on animal care and use (Austrian Federal Ministry for Science and Research). All methods were performed in accordance with the relevant guidelines and regulations. Animals were kept in a 12 h/12 h light/dark cycle, and all experiments were performed during circadian day times with light-adapted animals. All mice were anesthetized with isofluorane prior to cervical dislocation, decapitation, and tissue removal. Retinas (one sample = both retinas of one animal) were isolated from 3-month-old male C57BL6/J mice. Retinas were removed in cold PBS on ice and immediately transferred to the lysis buffer. Pineal glands (one sample = pineal glands of eight animals pooled) were extracted from 2- to 3-month-old female C57BL/6J mice. Pineal glands were collected from removed skullcaps and snap frozen in liquid nitrogen, stored at −80 °C, and subsequently pooled in the lysis step. Pancreatic islets (one sample = 145–197 islets per animal pooled) were collected from 2-month-old male C57BL/6N mice as described previously (50). Heart muscle (one sample = heart of one animal) was prepared from 2-month-old female C57BL/6J mice. Hearts were removed, and the caudal tips of the heart myocards were homogenized, with a rotor-stator homogenizer in lysis buffer followed by proteinase K digestion. Cochlea samples were taken from 3-week-old NMRI mice as part of another study (51). Samples from brain were dissected from 3-month-old male C57BL/6N mice as part of another study (52).

RNA isolation

RNA was isolated from the retina samples using Rneasy Mini kits (Qiagen). Contaminating genomic DNA was removed by Dnase I digestion (Qiagen) or prior to reverse transcription by dsDNase (Thermo). The isolated RNA concentrations and purities were determined on a Nanodrop spectrophotometer (Thermo).

Reverse transcription

For qPCR applications, reverse transcription of up to 1 μg of RNA was performed with Maxima H minus First Strand cDNA Synthesis kits (Thermo) using random hexamer primers or with LunaScript RT kits (NEB) using a mixture of random hexamer and oligo dT primers following manufacturer's instructions, and the resulting cDNAs were stored at −20 °C until use.

For 5′-RACE, PCR full-length cDNA was produced using the TeloPrime Full-Length cDNA Amplification Kit (Lexogen) using oligo-dT primers for reverse transcription and cap-dependent linker ligation selecting for mature full-length RNA molecules that are both polyadenylated and 5′-capped. During linker ligation, an adapter sequence (5′-TGGATTGATATGTAATACGACTCACTATAG-3′) was added to each full-length cDNA molecule, which was used for unbiased amplification of 5′ cDNA ends.

5′-RACE PCR

Two rounds of PCR in a seminested approach were used to amplify the 5′ end of Cavβ$_2$ transcripts. PCR products were visualized on 1.5% low-melting agarose gels together with a size marker (GeneRuler 1 kb Plus; Thermo). Gel-extracted bands (Monarch DNA gel extraction kit; NEB) from the first round were used as template for the second round. PCRs were run with a Phusion proof-reading polymerase using the primers summarized in Table 4 with following protocols:

Composition: 4 μl 5× high-fidelity buffer (Thermo), 2 μl dNTPs (2 mM), 0.6 μl dimethyl sulfoxide, 1 μl forward primer (10 μM), 1 μl reverse primer (10 μM), 0.2 μl Phusion polymerase (Thermo), 10.2 μl water, and 1 μl Cdna (20 ng) for the first round or 1 μl of purified gel–extracted PCR product of the first round for the second round. Program: 98 °C/30 s; [98 °C/7 s; T_m/27 s; 72 °C/25 s] * 35 cycles; 72 °C/10 min. T_m was 60 °C for the first round and 66 °C for the second round.

qPCR

Gene expression quantification was performed by probe-based qPCR using off the shelf and custom-made TaqMan assays (Thermo) for which standard curves were established as described elsewhere (53) to allow for absolute quantification. Most of the Cavβ TaqMan assays used have been established previously (54). Specificity of the new custom β_{2i} assay was confirmed by spike-in tests with mixtures of β_{2i}: β_{2a} DNA templates at 1:1, 1:2, 1:5, and 1:10 ratios (10^3:10^3 to 10^3:10^4 molecules) that showed unchanged cycle thresholds (C_T) from a pure β_{2i} template (C_T 27.34 for 10^3 molecules of pure β_{2i} *versus* C_T 27.63, 27.75, 27.82, and 27.93, respectively, for the mixtures; means, n = 3 each). qPCR was run on a real-time

Table 4
Primers for 5′-RACE PCR

PCR round	Forward primer	Reverse primer
First round	TGGATTGATATGTAATACGACTCACTATAG (TeloPrime adapter FOR)	GCACAGTTGGAAAAAGCAAAG (β_2 Ex3 REV out)
Second round	TGGATTGATATGTAATACGACTCACTATAG (TeloPrime adapter FOR)	CCGATTCAGATGTGTCTTTGG (β_2 Ex3 REV in)

Table 5
Assays for qPCR

Cavβ	Exon boundary	Assay ID or primer and probe sequences (5′-3′)
β_1	Ex1–Ex2	Mm00518940_m1
β_2	Ex4–Ex5	Mm01333550_m1
β_3	Ex1–Ex2	Mm00432233_m1
β_4	Ex11–Ex12	Mm00521623_m1
β_{2a}	5′-UTR—Ex2B	CACGGTGCCGCTTGGT (FOR) TGCATGAAGAGGTGGCAGAA (REV) AAGCCACGCTCTGAC (Probe)
β_{2b}	5′-UTR— Ex2C	TTACACATCTCAAACTTCAGGGAAAA (FOR) CCAGCTAAAGGTGGCTTTGC (REV) CGGAGCCCGTGCGA (Probe)
β_{2cd}[a]	Ex2A–Ex3	AAAGGCTCGGATGGAAGCA (FOR) CCCTGGCGGACAAAACTGT (REV) ATCGTCAGACACTACCTC (Probe)
β_{2e}	Ex2D—Ex3	GGGAGGAAGGCTGAAGAGTTC (FOR) GGGCGGCTGGTGTAGGA (REV) ACATCTGTGGTTCGGC (Probe)
β_{2i}	Ex2E–Ex3	AACTGCTGTTGGTCACCTCAACT (FOR) GGGCGGCTGGTGTAGGA (REV) TCCTGAATGTTGCCATGC (Probe)

Reference gene	Assay ID
Actb	Mm00607939_s1
B2m	Mm00437762_m1
Gapdh	Mm99999915_g1
Hprt1	Mm00446968_m1
Sdha	Mm01352363_m1
Tbp	Mm00446973_m1
Tfrc	Mm00441941_m1

[a] Assay does not distinguish between β_{2c} and β_{2d}.

PCR machine (7500 Fast Real-Time PCR System; Applied Biosystem) in duplicates in a 96-well format with the following composition per reaction: 10 µl Luna Universal Probe qPCR 2× master mix (NEB), 4 µl water, 1 µl assay, 5 µl Cdna (pre-adjusted to 0.4 ng/µl = 2 ng RNA-equivalent per reaction) or 5 µl water for negative controls, using the standard ramp speed program for probe-based assays. Cycle thresholds were determined at 0.1 ΔRn of the amplification curves, and molecule numbers were calculated as described before (55) based on the standard curves for each assay, normalized by the most stable reference (house-keeping) genes for each sample type determined by geNorm methods (56). The assays used are summarized in Table 5.

Cloning procedures

All β_2 vectors used in this study were based on plasmids containing the cds of mouse β_2 variants (β_{2a}:β_2-N3-Pcaggs-IRES-GFP, β_{2d}:β_2-N1-Pcaggs-IRES-GFP, β_{2e}:β_2-N5-Pcaggs-IRES-GFP; gift from V. Flockerzi (57)), thus using identical CAG promoters and differing only in the cds for the β_2 variants, ensuring equal drive for expression.

The β_2 variant expression vectors were supplemented with a DNA sequence coding for the C-terminal end of β_2 with the stop codon removed, a short linker (coding for Gly-Ala-Thr-Gly), and the cds for mEm (synthetic sequence; Twist BioScience) followed by a stop codon, leading to in-frame translation of β_2 variants with a C-terminally fused mEm fluorescent reporter for live-cell imaging experiments.

N-terminus modifications were derived from a synthetic DNA fragment (K>A, TS>A, and 10VL>A modifications; Twist BioScience) that introduced the desired changes by exchanging the respective part in the original β_{2i} vector. We generated β_{2X13} by replacing the HOOK domain in β_{2a} with the exon 7B-containing HOOK domain from β_{2i}. For electrophysiological experiments, β_2 variant vectors without conjugated reporter sequences were used. Where necessary, IRES-GFP cassettes were removed from parent β_2 variant vectors by SmaI digestion and religation of the backbones after gel purification.

Cloning β_{2i} from mouse retina

We used the full-length Cdna from whole mouse retina (as described previously) to amplify the β_{2i} sequence from N-terminus to exon 9 (including exon 7B) in a nested PCR approach (primers in Table 6). The nested forward primer added a SacI restriction site for subsequent cloning. PCR was run with the same composition and program described previously for the 5′-RACE PCR, albeit with 66 °C annealing temperature for the outer PCR and 61 °C for the nested PCR.

After gel electrophoresis, the bands with the predicted sizes were extracted using the Monarch DNA gel extraction kit (NEB) and used for nested PCR and restriction digestion, respectively. The nested PCR product was digested with SacI-HF and EcoRV-HF (NEB) yielding an insert with 5′ overhangs and a 3′ blunt end. The same enzymes were used to digest the target plasmid backbone (β_{2a}:β_2-N3-pCAGGS) into which the insert was ligated after purification by Takara DNA Ligation Kit (Takara) according to the manufacturer's instructions. Sequence identity was confirmed by sequencing.

Functional analyses in tsA-201 cells

Cell culture, transfection procedures, and whole-cell patch-clamp recording conditions were as previously described (58). Mouse β_2 subunits (mβ_{2i}-pCAGGS, mβ_{2X13}-pCAGGS, mβ_{2a}-pCAGGS-IRES-GFP, mβ_{2d}-pCAGGS, see aforementioned) were transiently cotransfected with human Cav1.4 α1 (59) and mouse $\alpha_2\delta$-4 (m$\alpha_2\delta$-4-pIRES2-enhanced GFP [eGFP] (60), gift from MA Denti/S Casarosa) or mouse β_2 subunits (mβ_{2i}-pCAGGS, m$\beta_{2i(K>A)}$-pCAGGS, m$\beta_{2i(5LV>A}$ first)-pCAGGS, m$\beta_{2i(10LV>A)}$-pCAGGS, mβ_{2a}-pCAGGS-IRES-GFP, and mβ_{2d}-pCAGGS) were transiently cotransfected with human Cav1.2

Table 6
Primers for cloning of mouse β_{2i}

PCR	Forward primer	Reverse primer	Size (bp)
Outer PCR	TGTGATGTGCAACTTTCCATG (5′UTR)	TTCACTCTGAACTTCCGCTAAG (exon 10–11 boundary)	1118
Nested PCR	AATT*GAGCTC*GCCACC**ATG**TTGGTGAAAC TGCTGTTGG (Ex2E; SacI; **start codon**)	TGATG*GATATC*CGCCCTTC (Exon 9–10 boundary; EcoRV)	863

α1 (61) and rabbit $\alpha_2\delta$-1 (GenBank accession number: NM_001082276) using the Ca^{2+}-phosphate precipitation method (62) together with eGFP as transfection marker in tsA-201 cells. DNA concentrations used for transfections were 0.2 μg/ml for β_2 subunits, 0.3 μg/ml Cav1.4 α1 or Cav1.2 α1, 0.25 μg/ml $\alpha_2\delta$-4, and 0.1 μg/ml eGFP, corresponding to ratios of approximately 0.9:1.0:0.6:0.5 for these vectors (DNA amounts normalized by plasmid sizes). Solutions for recordings were (in millimolar): intracellular solution: 135 CsCl, 10 Cs-EGTA, 1 $MgCl_2$, 10 Hepes, 4 Na_2-ATP, pH 7.3, adjusted with CsOH; extracellular solution: 15 $CaCl_2$ (for Cav1.4) or 15 $BaCl_2$ (for Cav1.2), 150 choline-Cl, 1 $MgCl_2$, 10 Hepes, pH 7.4 adjusted with CsOH. Borosilicate glass patch pipettes with resistances of 1.2 to 3.5 MΩ were used for recordings. Series resistance was compensated at 60 to 90%, data was low-pass filtered at 2 kHz, and digitized at 50 kHz sampling rate (Axopatch 200B, Digidata 1322A; Molecular Devices). I–V relationships were collected by 25 or 50 ms square pulse from the holding potential of −89 mV (liquid junction potentials of −9 mV corrected offline) to various test potentials (5 mV increments). The obtained I–V plots were fitted to the following equation:

$$I = G_{max} * (V - V_{rev}) / (1 + \exp(-(V - V_{0.5}) / k_{act}))$$

where G_{max} is the maximum slope conductance, V is the test potential, V_{rev} is the extrapolated reversal potential, $V_{0.5}$ is the voltage of half-maximal activation, and k_{act} is the activation slope factor. The VDI of the channels was examined by pulsing cells to V_{max} for 5 s from holding potential. The remaining current was quantified at the end of the test pulse as the percent of the peak inward current.

Cell culture for live-cell imaging

Round coverslips (13 mm diameter, thickness #1.5) were surface treated with hydrochloric acid, rinsed with water, sterilized with ethanol, dried and attached on a droplet of gelatine (1% in water) in 35 mm cell culture dishes before coating with poly-L-lysine (0.1 mg/ml). tsA-201 cells were seeded in the dishes with the prepared coverslips at 300,000 cells/dish and cultured and transfected as described previously using expression vectors of mEm-fused β_2 variants or a vector with mEm alone (0.15 μg plasmid DNA of each construct per dish, corresponding to 0.075 μg/ml). For some experiments, a marker for the Golgi apparatus was cotransfected (pmScarlet-H_Giantin_C1 was a gift from Dorus Gadella; Addgene plasmid #85049; http://n2t.net/addgene:85049; Research Resource Identifier: Addgene_85049 (63)). Cells were incubated 24 h post-transfection at 37 °C/5% CO_2 and in some experiments an additional 24 h at 30 °C/5% CO_2. Only cells from passages 9 to 18 were used for these experiments.

Live-cell imaging

Right before imaging, cell membranes (CellMask Deep Red plasma membrane stain, 1:2000 dilution in cell culture medium) and nuclei (4′,6-diamidino-2-phenylindole, 10 μg/ml) were stained for 10 min at 37 °C. Coverslips were washed thrice with PBS and mounted in PBS on glass slides for immediate live-cell imaging. Images were acquired on a Zeiss Axio Observer Z1 equipped with an ApoTome using a 63×/numerical aperture 1.4 Oil immersion objective and Colibri LED light source (excitation wavelengths 385 nm [4′,6-diamidino-2-phenylindole], 475 nm [mEm], 630 nm [CellMask Deep Red], 567 nm [mScarlet]) and appropriate filter sets for each fluorophore. A variable number of representative images with multiple mEm-positive cells per image were acquired from each coverslip and subjected to processing and analysis with the aim of highest possible comparability of conditions for evaluation.

Image processing and quantitative colocalization analysis

Zeiss Zen lite was used for image processing. Acquired images were divided into image sections containing cells with comparable mEm fluorescence intensity. The histograms of mEm and CellMask channels were adjusted to span the individual intensity ranges to achieve best possible comparability of the two markers and in between images. Colocalization analysis was performed using the plug-in JACoP (64) for ImageJ (https://imagej.nih.gov/ij/; Version 1.53q, Wayne Rasband, National Institutes of Health). The MC as measure of colocalization was calculated as the fraction of suprathreshold pixels in the mEm channel colocalizing with suprathreshold pixels in the CellMask channel, that is, percentage of mEm pixels localized at the membrane (10, 64). The thresholds for the calculation of the MC were set manually for the CellMask channel in each image aiming for best representation outline of the plasma membrane. The same threshold value was selected for the mEm channel to avoid bias and to ensure comparability (as both channel histograms had been preadjusted to span the same range). Image sections or individual cells were excluded from quantitative colocalization if at least one of the following criteria was fulfilled: dead cell, visible protrusions from the cell membrane, apparent overexposure, parts of the membrane blurry or weakly stained, and extracellular background fluorescence noise in the image indicating erroneous thresholds. Furthermore, image sections of cells expressing β_{2i} and modifications imaged 2 days post-transfection were excluded from quantification when strong reticular mEm signal or clusters in the Golgi apparatus above threshold were apparent.

Structure investigation

We downloaded all available Cavβ structures (Table 7) as well as full Ca^{2+} channel complex structures from the PDB aligned and visualized them with PyMOL (The PyMOL Molecular Graphics System, Version 1.8.0.0; Schrödinger, LLC) and UniProt Align (https://www.uniprot.org/align; European Molecular Biology Laboratory, EMBL) (65, 66).

Table 7
Available β_2 structures

PDB code	Mzethod	Resolution (Å)	Species	Reference
1T0H	X-ray	1.97	*Rattus norvegicus* (rat)	(21)
1T0J	X-ray	2.00	*Rattus norvegicus* (rat)	(21)
1T3L	X-ray	2.20	*Oryctolagus cuniculus* (rabbit)	(26)
1T3S	X-ray	2.30	*Oryctolagus cuniculus* (rabbit)	(26)
3JBR	Cryo-EM	4.20	*Rattus norvegicus* (rat)	(29)
4DEX	X-ray	2.00	*Oryctolagus cuniculus* (rabbit)	(68)
4DEY	X-ray	1.95	*Oryctolagus cuniculus* (rabbit)	(68)
5V2P	X-ray	2.00	*Rattus norvegicus* (rat)	(69)
5V2Q	X-ray	1.70	*Rattus norvegicus* (rat)	(69)

All structures based on β_{2a} constructs (3JBR docked β_{2a} [1T0J] in place of β_{1a}).
Abbreviation: X-ray, X-ray crystallography.

Statistical analysis

Electrophysiology

Data are presented as mean ± SD, unless stated otherwise for the indicated number of cells analyzed (n). Data analysis was performed using Clampfit 10.0 (Axon Instruments), Sigmaplot 14.0 (Systat), and GraphPad Prism 8.0 (GraphPad Software, Inc). Data were statistically analyzed by one-way ANOVA with multiple comparisons in reference to β_{2i} in GraphPad Prism 8.0. Statistical significance was set at $p < 0.05$. Significance levels of $p < 0.05$, $p < 0.01$, or $p < 0.001$ are denoted in graphs by a single, double, or triple asterisk, respectively. Inactivation properties were determined as remaining currents after 5000 ms as a percentage of the maximum (r5000)

Live-cell imaging

The arithmetic mean of the MCs was calculated for each transfection (n). These means were weighted against the number of analyzed image sections per transfection to calculate the weighted mean over transfections. Statistical analyses were done in GraphPad Prism. Data were analyzed by one-way ANOVA with multiple comparisons in reference to β_{2i}. Statistical significance was set at $p < 0.05$. Significance levels of $p < 0.05$, $p < 0.01$, or $p < 0.001$ are denoted in graphs and tables by a single, double, or triple asterisk, respectively.

Data availability

All data generated or analyzed during this study are included in this published article (and its supporting information files).

Supporting information—This article contains supporting information (11, 13, 30, 50–52, 66, 69–76).

Acknowledgments—We thank Thomas Heigl for outstanding scientific support, Bettina Tschugg and Jennifer Müller for excellent technical support, Filip Van Petegem for fruitful discussion, and Noelia Jacobo-Piqueras and Nadja Hofer for aid in preparation of mouse tissue samples. This work was supported by the Center for Molecular Biosciences Innsbruck, the University of Innsbruck, and the Medical University of Innsbruck.

Author contributions—H. S. and A. K. conceptualization; H. S., J. O., J. H., L. Z., U. T. L., G. F., M. L. F.-Q., and T. K. methodology; G. F. and M. L. F.-Q. software; H. S., J. O., P. G., J. H., L. Z., G. F., M. L. F.-Q., and T. K. formal analysis; J. O., P. G., J. H., L. Z., and U. T. L. investigation; H. S., L. Z., and A. K. validation; H. S. and A. K. writing–original draft; H. S., J. O., P. G., U. T. L., G. F., M. L. F.-Q., T. K., and A. K. writing–review & editing; H. S., J. O., P. G., J. H., L. Z., G. F., M. L. F.-Q., and T. K. visualization; H. S. and A. K. project administration; H. S. and A. K. funding acquisition.

Funding and additional information—This research was funded in whole, or in part, by the Austrian Science Fund (FWF P33566 to H. S. and P32747 to A. K.). For the purpose of open access, the author has applied a CC BY public copyright licence to any author accepted manuscript version arising from this submission.

Conflict of interest—The authors declare that they have no conflicts of interest with the contents of this article.

Abbreviations—The abbreviations used are: cDNA, complementary DNA; cds, coding sequence; eGFP, enhanced GFP; ER, endoplasmic reticulum; GEO, Gene Expression Omnibus; GK, guanylate kinase-like; IGV, Integrative Genomics Viewer; I–V, current–voltage; MC, Mander's coefficient; mEm, mEmerald; PDB, Protein Data Bank; qPCR, quantitative real-time PCR; RACE, rapid amplication of cDNA end; SH3, Src homology 3; VDI, voltage-dependent inactivation; VGCC, voltage-gated Ca^{2+} channel.

References

1. Neely, A., Garcia-Olivares, J., Voswinkel, S., Horstkott, H., and Hidalgo, P. (2004) Folding of active calcium channel β1b-subunit by size-exclusion chromatography and its role on channel function. *J. Biol. Chem.* **279**, 21689–21694
2. Buraei, Z., and Yang, J. (2013) Structure and function of the β subunit of voltage-gated Ca2+ channels. *Biochim. Biophys. Acta* **1828**, 1530–1540
3. Olcese, R., Qin, N., Schneider, T., Neely, A., Wei, X., Stefani, E., *et al.* (1994) The amino terminus of a calcium channel β subunit sets rates of channel inactivation independently of the subunit's effect on activation. *Neuron* **13**, 1433–1438
4. Qin, N., Olcese, R., Zhou, J., Cabello, O. A., Birnbaumer, L., and Stefani, E. (1996) Identification of a second region of the β-subunit involved in regulation of calcium channel inactivation. *Am. J. Physiol.* **271**, C1539–C1545
5. Buraei, Z., and Yang, J. (2010) The ß subunit of voltage-gated Ca2+ channels. *Physiol. Rev.* **90**, 1461–1506
6. Campiglio, M., and Flucher, B. E. (2015) The role of auxiliary subunits for the functional diversity of voltage-gated calcium channels. *J. Cell. Physiol.* **230**, 2019–2031
7. Dolphin, A. C. (2012) Calcium channel auxiliary α2δ and β subunits: trafficking and one step beyond. *Nat. Rev. Neurosci.* **13**, 542–555
8. Chien, A. J., Gao, T., Perez-Reyes, E., and Hosey, M. M. (1998) Membrane targeting of L-type calcium channels. *J. Biol. Chem.* **273**, 23590–23597

9. Qin, N., Platano, D., Olcese, R., Costantin, J. L., Stefani, E., and Birnbaumer, L. (1998) Unique regulatory properties of the type 2a Ca2+ channel β subunit caused by palmitoylation. *Proc. Natl. Acad. Sci. U. S. A.* **95**, 4690–4695
10. Miranda-laferte, E., Ewers, D., Guzman, R. E., Jordan, N., Schmidt, S., and Hidalgo, P. (2014) The N-terminal domain tethers the voltage-gated calcium channel β2e-subunit to the plasma membrane via electrostatic and hydrophobic. *J. Biol. Chem.* **289**, 10387–10398
11. Lee, A., Wang, S., Williams, B., Hagen, J., Scheetz, T. E., and Haeseleer, F. (2015) Characterization of Cav1.4 complexes (α1 1.4, β2, and α2δ4) in HEK293T cells and in the retina. *J. Biol. Chem.* **290**, 1505–1521
12. Brooks, M. J., Rajasimha, H. K., Roger, J. E., and Swaroop, A. (2011) Next-generation sequencing facilitates quantitative analysis of wild-type and Nrl retinal transcriptomes. *Mol. Vis.* **17**, 3034–3054
13. Chang, E., Fu, C., Coon, S. L., Alon, S., Bozinoski, M., Breymaier, M., *et al.* (2020) Resource: a multi-species multi-timepoint transcriptome database and webpage for the pineal gland and retina. *J. Pineal Res.* **69**, e12673
14. Takahashi, S. X., Mittman, S., and Colecraft, H. M. (2003) Distinctive modulatory effects of five human auxiliary β2 subunit splice variants on L-type calcium channel gating. *Biophys. J.* **84**, 3007–3021
15. Restituito, S., Cens, T., Barrere, C., Geib, S., Galas, S., de Waard, M., *et al.* (2000) The β_{2a} subunit is a molecular groom for the Ca^{2+} channel inactivation gate. *J. Neurosci.* **20**, 9046–9052
16. Chien, A. J., Carr, K. M., Shirokov, R. E., Rios, E., and Marlene Hosey, M. (1996) Identification of palmitoylation sites within the L-type calcium channel β(2a) subunit and effects on channel function. *J. Biol. Chem.* **271**, 26465–26468
17. Koschak, A., Reimer, D., Walter, D., Hoda, J.-C., Heinzle, T., Grabner, M., *et al.* (2003) Cav1.4alpha1 subunits can form slowly inactivating dihydropyridine-sensitive L-type Ca2+ channels lacking Ca2+-dependent inactivation. *J. Neurosci.* **23**, 6041–6049
18. Koschak, A., Reimer, D., Huber, I., Grabner, M., Glossmann, H., Engel, J., *et al.* (2001) α1D (Cav1.3) subunits can form L-type Ca2+ channels activating at negative voltages. *J. Biol. Chem.* **276**, 22100–22106
19. Ortner, N. J., Bock, G., Dougalis, A., Kharitonova, M., Duda, J., Hess, S., *et al.* (2017) Lower affinity of isradipine for L-type Ca2+ channels during substantia nigra dopamine neuron-like activity: implications for neuroprotection in Parkinson's disease. *J. Neurosci.* **37**, 6761–6777
20. Seibel, N. M., Eljouni, J., Nalaskowski, M. M., and Hampe, W. (2007) Nuclear localization of enhanced green fluorescent protein homomultimers. *Anal. Biochem.* **368**, 95–99
21. Van Petegem, F., Clark, K. A., Chatelain, F. C., and Minor, D. L. (2004) Structure of a complex between a voltage-gated calcium channel β-subunit and an α-subunit domain. *Nature* **429**, 671–675
22. Opatowsky, Y., Chomsky-Hecht, O., Kang, M.-G., Campbell, K. P., and Hirsch, J. A. (2003) The voltage-dependent calcium channel β subunit contains two stable interacting domains. *J. Biol. Chem.* **278**, 52323–52332
23. Norris, N. C., Joseph, S., Aditya, S., Karunasekara, Y., Board, P. G., Dulhunty, A. F., *et al.* (2017) Structural and biophysical analyses of the skeletal dihydropyridine receptor β subunit β1a reveal critical roles of domain interactions for stability. *J. Biol. Chem.* **292**, 8401–8411
24. Zhao, Y., Huang, G., Wu, J., Wu, Q., Gao, S., Yan, Z., *et al.* (2019) Molecular basis for ligand modulation of a mammalian voltage-gated Ca2+ channel. *Cell* **177**, 1495–1506.e12
25. Dong, Y., Gao, Y., Xu, S., Wang, Y., Yu, Z., Li, Y., *et al.* (2021) Closed-state inactivation and pore-blocker modulation mechanisms of human CaV2.2. *Cell Rep.* **37**, 109931
26. Opatowsky, Y., Chen, C.-C., Campbell, K. P., and Hirsch, J. A. (2004) Structural analysis of the voltage-dependent calcium channel β subunit functional core and its complex with the α1 interaction domain. *Neuron* **42**, 387–399
27. Vendel, A. C. (2006) Solution structure of the N-terminal A domain of the human voltage-gated Ca2+channel beta4a subunit. *Protein Sci.* **15**, 378–383
28. Lomize, M. A., Pogozheva, I. D., Joo, H., Mosberg, H. I., and Lomize, A. L. (2012) OPM database and PPM web server: resources for positioning of proteins in membranes. *Nucleic Acids Res.* **40**, D370–D376
29. Wu, J., Yan, Z., Li, Z., Yan, C., Lu, S., Dong, M., *et al.* (2015) Structure of the voltage-gated calcium channel Ca_v1.1 complex. *Science* **350**, aad2395
30. Jumper, J., Evans, R., Pritzel, A., Green, T., Figurnov, M., Ronneberger, O., *et al.* (2021) Highly accurate protein structure prediction with AlphaFold. *Nature* **596**, 583–589
31. Popova, E. Y., Salzberg, A. C., Yang, C., Zhang, S. S.-M., and Barnstable, C. J. (2017) Identification and prediction of alternative transcription start sites that generate rod photoreceptor-specific transcripts from ubiquitously expressed genes. *PLoS One* **12**, e0179230
32. Benitez-Cantos, M. S., Yordanova, M. M., O'Connor, P. B. F., Zhdanov, A. V., Kovalchuk, S. I., Papkovsky, D. B., *et al.* (2020) Translation initiation downstream from annotated start codons in human mRNAs co-evolves with the Kozak context. *Genome Res.* **30**, 974–984
33. Jeckelmann, J.-M., and Erni, B. (2020) Transporters of glucose and other carbohydrates in bacteria. *Pflugers Arch.* **472**, 1129–1153
34. Colecraft, H. M., Alseikhan, B., Takahashi, S. X., Chaudhuri, D., Mittman, S., Yegnasubramanian, V., *et al.* (2002) Novel functional properties of Ca(2+) channel beta subunits revealed by their expression in adult rat heart cells. *J. Physiol.* **541**, 435–452
35. Dzhura, I., and Neely, A. (2003) Differential modulation of cardiac Ca2+ channel gating by beta-subunits. *Biophys. J.* **85**, 274–289
36. Suh, B. C., Kim, D.il, Falkenburger, B. H., and Hille, B. (2012) Membrane-localized β-subunits alter the PIP 2 regulation of high-voltage activated Ca 2+ channels. *Proc. Natl. Acad. Sci. U. S. A.* **109**, 3161–3166
37. Richards, M. W., Leroy, J., Pratt, W. S., and Dolphin, A. C. (2007) The HOOK-domain between the SH3 and the GK domains of Cavbeta subunits contains key determinants controlling calcium channel inactivation. *Channels (Austin)* **1**, 92–101
38. Tan, G. M. Y., Yu, D., Wang, J., and Soong, T. W. (2012) Alternative splicing at C terminus of Ca v1.4 calcium channel modulates calcium-dependent inactivation, activation potential, and current density. *J. Biol. Chem.* **287**, 832–847
39. Babai, N., Morgans, C. W., and Thoreson, W. B. (2010) Calcium-induced calcium release contributes to synaptic release from mouse rod photoreceptors. *Neuroscience* **165**, 1447–1456
40. Mercurio, A. M., and Holtzman, E. (1982) Smooth endoplasmic reticulum and other agranular reticulum in frog retinal photoreceptors. *J. Neurocytol.* **11**, 263–293
41. Miranda-Laferte, E., Gonzalez-Gutierrez, G., Schmidt, S., Zeug, A., Ponimaskin, E. G., Neely, A., *et al.* (2011) Homodimerization of the Src homology 3 domain of the calcium channel β-subunit drives dynamin-dependent endocytosis. *J. Biol. Chem.* **286**, 22203–22210
42. Lao, Q. Z., Kobrinsky, E., Liu, Z., and Soldatov, N. M. (2010) Oligomerization of Cavbeta subunits is an essential correlate of Ca2+ channel activity. *FASEB J.* **24**, 5013–5023
43. Kiyonaka, S., Wakamori, M., Miki, T., Uriu, Y., Nonaka, M., Bito, H., *et al.* (2007) RIM1 confers sustained activity and neurotransmitter vesicle anchoring to presynaptic Ca2+ channels. *Nat. Neurosci.* **10**, 691–701
44. Alberts, B., Johnson, A., and Lewis, J. (2002) *Molecular Biology of the Cell*, 4th Ed, Garland Science, New York, NY
45. Fuglebakk, E., and Reuter, N. (2018) A model for hydrophobic protrusions on peripheral membrane proteins. *PLoS Comput. Biol.* **14**, e1006325
46. Bolger, A. M., Lohse, M., and Usadel, B. (2014) Trimmomatic: a flexible trimmer for illumina sequence data. *Bioinformatics* **30**, 2114–2120
47. Dobin, A., Davis, C. A., Schlesinger, F., Drenkow, J., Zaleski, C., Jha, S., *et al.* (2013) STAR: ultrafast universal RNA-seq aligner. *Bioinformatics* **29**, 15–21
48. Liao, Y., Smyth, G. K., and Shi, W. (2014) featureCounts: an efficient general purpose program for assigning sequence reads to genomic features. *Bioinformatics* **30**, 923–930
49. Robinson, J. T., Thorvaldsdóttir, H., Winckler, W., Guttman, M., Lander, E. S., Getz, G., *et al.* (2011) Integrative genomics viewer. *Nat. Biotechnol.* **29**, 24–26
50. Mastrolia, V., Flucher, S. M., Obermair, G. J., Drach, M., Hofer, H., Renström, E., *et al.* (2017) Loss of α2δ-1 calcium channel subunit function increases the susceptibility for diabetes. *Diabetes* **66**, 897–907

51. Ortner, N. J., Pinggera, A., Hofer, N. T., Siller, A., Brandt, N., Raffeiner, A., *et al.* (2020) RBP2 stabilizes slow Cav1.3 Ca2+ channel inactivation properties of cochlear inner hair cells. *Pflugers Arch.* **472**, 3–25
52. Hofer, N. T., Pinggera, A., Nikonishyna, Y.v., Tuluc, P., Fritz, E. M., Obermair, G. J., *et al.* (2021) Stabilization of negative activation voltages of Cav1.3 L-Type Ca2+-channels by alternative splicing. *Channels (Austin)* **15**, 38–52
53. Schlick, B., Flucher, B. E., and Obermair, G. J. (2010) Voltage-activated calcium channel expression profiles in mouse brain and cultured hippocampal neurons. *Neuroscience* **167**, 786–798
54. Siller, A., Hofer, N. T., Tomagra, G., Burkert, N., Hess, S., Benkert, J., *et al.* (2022) β2-subunit alternative splicing stabilizes Cav2.3 Ca2+ channel activity during continuous midbrain dopamine neuron-like activity. *Elife* **11**, e67464
55. Knoflach, D., Kerov, V., Sartori, S. B., Obermair, G. J., Schmuckermair, C., Liu, X., *et al.* (2013) Cav1.4 IT mouse as model for vision impairment in human congenital stationary night blindness type 2. *Channels* **7**, 37–41
56. Vandesompele, J., de Preter, K., Pattyn, F., Poppe, B., van Roy, N., de Paepe, A., *et al.* (2002) Accurate normalization of real-time quantitative RT-PCR data by geometric averaging of multiple internal control genes. *Genome Biol.* **3**, RESEARCH0034
57. Link, S., Meissner, M., Held, B., Beck, A., Weissgerber, P., Freichel, M., *et al.* (2009) Diversity and developmental expression of L-type calcium channel beta2 proteins and their influence on calcium current in murine heart. *J. Biol. Chem.* **284**, 30129–30137
58. Zanetti, L., Kilicarslan, I., Netzer, M., Babai, N., Seitter, H., and Koschak, A. (2021) Function of cone and cone-related pathways in CaV1.4 IT mice. *Sci. Rep.* **11**, 2732
59. Burtscher, V., Schicker, K., Novikova, E., Pöhn, B., Stockner, T., Kugler, C., *et al.* (2014) Spectrum of Cav1.4 dysfunction in congenital stationary night blindness type 2. *Biochim. Biophys. Acta* **1838**, 2053–2065
60. Bacchi, N., Messina, A., Burtscher, V., Dassi, E., Provenzano, G., Bozzi, Y., *et al.* (2015) A new splicing isoform of Cacna2d4 mimicking the effects of c.2451insC mutation in the retina: novel molecular and electrophysiological insights. *Invest. Ophthalmol. Vis. Sci.* **56**, 4846–4856
61. Liao, P., Yu, D., Li, G., Yong, T. F., Soon, J. L., Chua, Y. L., *et al.* (2007) A smooth muscle Cav1.2 calcium channel splice variant underlies hyperpolarized window current and enhanced state-dependent inhibition by nifedipine. *J. Biol. Chem.* **282**, 35133–35142
62. Singh, A., Gebhart, M., Fritsch, R., Sinnegger-Brauns, M. J., Poggiani, C., Hoda, J.-C., *et al.* (2008) Modulation of voltage- and Ca2+-dependent gating of CaV1.3 L-type calcium channels by alternative splicing of a C-terminal regulatory domain. *J. Biol. Chem.* **283**, 20733–20744
63. Bindels, D. S., Haarbosch, L., van Weeren, L., Postma, M., Wiese, K. E., Mastop, M., *et al.* (2017) mScarlet: a bright monomeric red fluorescent protein for cellular imaging. *Nat. Methods* **14**, 53–56
64. Bolte, S., and Cordelières, F. P. (2006) A guided tour into subcellular colocalization analysis in light microscopy. *J. Microsc.* **224**, 213–232
65. Sievers, F., Wilm, A., Dineen, D., Gibson, T. J., Karplus, K., Li, W., *et al.* (2011) Fast, scalable generation of high-quality protein multiple sequence alignments using Clustal Omega. *Mol. Syst. Biol.* **7**, 539
66. Madeira, F., Pearce, M., Tivey, A. R. N., Basutkar, P., Lee, J., Edbali, O., *et al.* (2022) Search and sequence analysis tools services from EMBL-EBI in 2022. *Nucleic Acids Res.* **50**, W276–W279
67. Findeisen, F., Campiglio, M., Jo, H., Abderemane-Ali, F., Rumpf, C. H., Pope, L., *et al.* (2017) Stapled voltage-gated calcium channel (Ca $_V$) α-interaction domain (AID) peptides act as selective protein–protein interaction inhibitors of Ca $_V$ function. *ACS Chem. Neurosci.* **8**, 1313–1326
68. Almagor, L., Chomsky-Hecht, O., Ben-Mocha, A., Hendin-Barak, D., Dascal, N., and Hirsch, J. A. (2012) The role of a voltage-dependent Ca2+ channel intracellular linker: a structure-function analysis. *J. Neurosci.* **32**, 7602–7613
69. Hartl, D., Krebs, A. R., Jüttner, J., Roska, B., and Schübeler, D. (2017) Cis-regulatory landscapes of four cell types of the retina. *Nucleic Acids Res.* **45**, 11607–11621
70. Shekhar, K., Lapan, S. W., Whitney, I. E., Tran, N. M., Macosko, E. Z., Kowalczyk, M., *et al.* (2016) Comprehensive classification of retinal bipolar neurons by single-cell transcriptomics. *Cell* **166**, 1308–1323.e30
71. Farkas, M. H., Grant, G. R., White, J. A., Sousa, M. E., Consugar, M. B., and Pierce, E. A. (2013) Transcriptome analyses of the human retina identify unprecedented transcript diversity and 3.5 Mb of novel transcribed sequence via significant alternative splicing and novel genes. *BMC Genomics* **14**, 486
72. Feodorova, Y., Koch, M., Bultman, S., Michalakis, S., and Solovei, I. (2015) Quick and reliable method for retina dissociation and separation of rod photoreceptor perikarya from adult mice. *MethodsX* **2**, 39–46
73. Davison, A., Lux, U. T., Brandstätter, J. H., and Babai, N. (2022) T-type Ca2+ channels boost neurotransmission in mammalian cone photoreceptors. *J. Neurosci.* **42**, 6325–6343
74. Zhang, X. M., Chen, B. Y., Ng, A. H. L., Tanner, J. A., Tay, D., So, K. F., *et al.* (2005) Transgenic mice expressing Cre-recombinase specifically in retinal rod bipolar neurons. *Invest. Ophthalmol. Vis. Sci.* **46**, 3515–3520
75. Crooks, G. E., Hon, G., Chandonia, J.-M., and Brenner, S. E. (2004) WebLogo: a sequence logo generator. *Genome Res.* **14**, 1188–1190
76. Johnson, M., Zaretskaya, I., Raytselis, Y., Merezhuk, Y., McGinnis, S., and Madden, T. L. (2008) NCBI BLAST: a better web interface. *Nucleic Acids Res.* **36**, W5–W9